

1  
2 Convective hydration in the tropical tropopause layer during the StratoClim aircraft campaign:  
3 Pathway of an observed hydration patch

4  
5 Keun-Ok Lee<sup>1</sup>, Thibaut Dauhut<sup>1</sup>, Jean-Pierre Chaboureau<sup>1</sup>, Sergey Khaykin<sup>2</sup>, Martina Krämer<sup>3</sup> and  
6 Christian Rolf<sup>3</sup>

7 <sup>1</sup>Laboratoire d'Aérodynamique, Université de Toulouse, CNRS, UPS, Toulouse, France

8 <sup>2</sup> LATMOS-IPSL, Université Versailles St-Quentin; Sorbonne Université, CNRS/INSU, Guyancourt, France

9 <sup>3</sup>Institute for Energy and Climate Research – Stratosphere (IEK-7), Forschungszentrum Jülich, Jülich, Germany

10  
11 ABSTRACT

12 The source and pathway of the hydration patch in the TTL (Tropical Tropopause Layer) that was measured  
13 during the StratoClim field campaign during the Asian summer monsoon in 2017, and its connection to  
14 convective overshoots are investigated. During flight #7, two remarkable layers are measured in the TTL  
15 namely, (1) moist layer (ML) with water vapour content of 4.8–5.7 ppmv in altitudes of 18–19 km altitudes in  
16 the lower stratosphere, and (2) ice layer (IL) with ice content up to 1.9 eq. ppmv in altitudes of 17–18 km in  
17 the upper troposphere around 06:30 UTC on 8 August to the south of Kathmandu (Nepal). A Meso-NH  
18 convection-permitting simulation succeeds in reproducing the characteristics of ML and IL. Through analysis,  
19 we show that ML and IL are generated by convective overshoots that occurred over the Sichuan basin about  
20 1.5 day before. Overshooting clouds develop up to 19 km, hydrating the lower stratosphere of up to 20 km  
21 with 6401 t of water vapour by a strong-to-moderate mixing of the updraughts with the stratospheric air. A few  
22 hours after the initial overshooting phase, a hydration patch is generated, and a large amount of water vapour  
23 (above 18 ppmv) remained at even higher altitudes up to 20.5 km while the anvil cloud top descends to 18.5  
24 km. At the same time, a great part of the hydrometeors falls shortly, and the water vapour concentration in ML  
25 and IL decreases due to turbulent diffusion by mixing with the tropospheric air and in-situ ice microphysics.  
26 As the hydration patch continues to travel toward the south of Kathmandu, tropospheric tracer concentration  
27 increases up to ~30 and 70 % in ML and IL, respectively. The air mass in the layers becomes gradually diffused  
28 and it has less and less water vapour and ice content by mixing with the dry tropospheric air.

30

## 31 **1. Introduction**

32 The Asian summer monsoon anticyclone is one of the most pronounced circulation patterns in the Northern  
33 Hemisphere, and it is a dominant climatological feature of the global circulation during boreal summer (Mason  
34 and Anderson, 1963; Randel and Park, 2006). The monsoon circulation horizontally covers large parts of  
35 southern Asia and the Middle East, and is located on the edge of the tropics and subtropics. It consists of  
36 cyclonic flow and convergence in the lower troposphere together with strong anticyclonic circulation and  
37 divergence in the upper troposphere. This circulation is coupled with persistent deep convection over the south  
38 Asia region during summer (June to September) (Hoskins and Rodwell, 1995). The monsoon tropopause is  
39 relatively high at about 4.2 ppmv; the upper tropospheric anticyclonic circulation extends into the lower  
40 stratosphere spanning from around 300 hPa and 70 hPa, i.e. approximately the whole upper troposphere and  
41 lower stratosphere (UTLS) (Highwood and Hoskins, 1998; Randel and Park, 2006).

42 Due to the strong dynamical signature in the UTLS, the influence of the monsoon is evident in chemical  
43 constituents, i.e. water vapour is relatively high at about 4.2 ppmv (Wright et al., 2011), ozone is relatively low  
44 (Randel et al., 2001), and methane, nitrogen oxides, and carbon monoxide are relatively high (Park et al., 2004;  
45 Li et al., 2005). Especially, the water vapour in the UTLS is controlled by the troposphere-to-stratosphere  
46 transport of moisture across the tropical tropopause layer (TTL, located between ~150 hPa (355 K, 14 km) and  
47 ~70 hPa (425 K, 18.5 km); Fueglistaler et al., 2009; Rolf et al., 2018). It is mainly driven by the large-scale  
48 cold point tropopause temperature field, but also processes involving convection, gravity waves, and cirrus  
49 cloud microphysics that modulate TTL humidity.

50 Convective overshoots that penetrate the tropopause directly inject air and water into the stratosphere.  
51 Fundamentally, convection arises from the temperature difference between a parcel of warm air and the cooler  
52 air surrounding it. Warm air, which is less dense, i.e. more buoyant, rises through the atmospheric column and  
53 adiabatically expands and cools. When the temperature of the rising air parcel has cooled sufficiently, the water  
54 vapour it contains will begin to condense and release latent heat. If air parcels within the convective core have  
55 enough upward momentum, they continue to rise beyond their equilibrium level of zero buoyancy, and form  
56 overshoots. They eventually form an overshoot that penetrate into the lowermost stratosphere by crossing the  
57 cold point tropopause. The convective overshoots have the potential to increase the humidity in the stratosphere  
58 via rapid sublimation of convectively lofted ice and mixing with dry stratospheric air. This has been

59 demonstrated in previous studies in both modelling and measurement (Dessler and Sherwood, 2004;  
60 Chaboureau et al., 2007; Jensen et al., 2007; Homeyer et al., 2014; Khaykin et al., 2016; Rysman et al., 2016;  
61 Homeyer et al., 2017; Smith et al., 2017; Dauhut et al., 2018; Funatsu et al., 2018; among others). Even a small  
62 volume of tropospheric air can carry a significant quantity of water in the condensed phase. Mixing of  
63 tropospheric air with the surrounding stratosphere, which is typically sub-saturated, facilitates the rapid  
64 sublimation of lofted ice. Also, the origin of the injected water to the TTL has been studied by backward  
65 trajectory analysis at global scale, and it was found that the convective sources are generally higher over the  
66 continental part of the Asian monsoon region in comparison to other tropical regions, with shorter transit times  
67 (Tzella and Legras, 2005; Tissier and Legras, 2016). However, the net contribution of convective overshoots  
68 to stratospheric water vapour concentration is not well understood at mesoscale and is not well represented in  
69 global models because of the small spatial scales (less than a few kilometres) and short time scales (less than  
70 few hours) over which convection occurs.

71 The tropical aircraft campaign of the Stratospheric and upper tropospheric processes for better Climate  
72 predictions (StratoClim, [www.stratoclim.org](http://www.stratoclim.org)) took place in summer 2017. It aimed to improve our knowledge  
73 of the key processes, i.e. microphysical, chemical and dynamical processes, which determine the composition  
74 of the UTLS, such as the formation, loss, and redistribution of chemical constituents (water vapour, ozone, and  
75 aerosol). During the campaign, eight dedicated flights were successfully operated with the objective of  
76 documenting the connection between the moisture plumes in the UTLS and the convective sources from south  
77 Kathmandu, Nepal, during summer monsoon season.

78 Our study focuses on part of flight #7 to the south of Kathmandu measuring the stratospheric hydration  
79 in the altitudes between 17 and 19 km. The objective of our work is to investigate the source and pathway of  
80 the localized moisture in the TTL that was measured by aircraft in connection to a convective overshoot. This  
81 is done using a combination of airborne and spaceborne observations as well as a convection-permitting  
82 simulation performed with a fine resolution in the TTL.

83 A detailed description of the dataset is given in section 2. Section 3 presents the moistened TTL signature  
84 captured by airborne and spaceborne observations and the numerical simulation. Section 4 demonstrates the  
85 convective origin of the enhanced moisture and shows its evolution along its path in the lower stratosphere. A  
86 summary and discussion of the findings of the present study are given in section 5.

87

88

## 89 **2. Data and method**

90 M55-Geophysica aircraft deployment in Kathmandu during Asian Summer Monsoon in July-August 2017  
91 provided unprecedented sampling of the UTLS region above the southern slopes of Himalayas. More details  
92 concerning the observational datasets used in this study together with the airborne and spaceborne  
93 measurements and the convection-permitting simulation are provided in the following.

94

### 95 *2.1. StratoClim airborne observations*

96 During flight #7, the M55-Geophysica aircraft flew back and forth between Kathmandu in Nepal and west  
97 Bengal in India (for the track, see the red line in Fig. 1) from 04:30 UTC to 06:50 UTC on 8 August 2017. In-  
98 situ sensor onboard the aircraft measures the relative humidity with respect to ice (hereafter called simply  
99 ‘relative humidity’ or ‘RH<sub>ice</sub>’), temperature and wind speed and direction every 1 second. FLASH and FISH  
100 instruments on board the Geophysica aircraft sampled the vertical water vapour and ice content distribution  
101 every 1 second, respectively.

102 FLASH-A (Fluorescent Lyman-Alpha Stratospheric Hygrometer for Aircraft) is an advanced version of  
103 the airborne FLASH instrument (Sitnikov et al, 2007; Khaykin et al., 2013) previously flown onboard the  
104 M55-Geophysica aircraft. FLASH-A has a rear facing inlet allowing measurement of gas-phase water in the  
105 altitude range between 12–21 km, with the latter being the aircraft ceiling altitude. Total uncertainty of water  
106 vapour measurement amounts to 9 % with a detection limit of 0.2 ppmv, whereas the measurement precision  
107 at 1 Hz sampling is better than 6 %.

108 FISH (Fast In situ Stratospheric Hygrometer) is a closed-path Lyman- $\alpha$  photo fragment fluorescence  
109 hygrometer that measures total water (sum of gas phase and evaporated ice crystals) in the range of 1–1000  
110 ppmv between 50 and 500 hPa levels with an accuracy and precision of 6–8 % and 0.3 ppmv (Zöger et al.,  
111 1999; Meyer et al., 2015). The time resolution of the measurements is 1 Hz. Inside of ice clouds, ice water  
112 content (IWC) is calculated by subtracting the gas phase water measured by FLASH from the total water  
113 detected by FISH as described by Afchine et al. (2018). The minimum detectable IWC is  $3 \times 10^{-2}$  ppmv  
114 ( $\sim 3 \times 10^{-3}$  mg m<sup>-3</sup>).

115

## 116 *2.2. Spaceborne observation*

117 Calibrated thermal infrared brightness temperature (BT) data at 10.8  $\mu\text{m}$  wavelength, acquired every 15 min  
118 by the Spinning Enhanced Visible and Infrared Imager (SEVIRI) onboard the geostationary Meteosat Second  
119 Generation satellite (MSG) were employed to investigate the evolution of deep convection. The spatial  
120 resolution of the MSG-SEVIRI data used is  $0.05^\circ$  in both latitude and longitude. BT minima are generally  
121 indicative of the cloud top overshoots associated with deep convection (e.g. Kato, 2006).

122 Vertical profiles of backscatter retrieved from the Cloud-Aerosol Lidar with Orthogonal Polarization  
123 (CALIOP) on board CALIPSO (Winker et al. 2009) with a wavelength at 532 nm are used. CALIOP provides  
124 observations of particles, including high clouds, with a very high sampling resolution, 30 and 335 m in the  
125 vertical and horizontal directions, respectively.

126

## 127 *2.3. Cloud-resolving numerical simulation*

128 The target convective overshoots and the moistened TTL were simulated using the non-hydrostatic numerical  
129 research model, Meso-NH (Lac et al. 2018). For a fine-scale analysis, the simulation uses about 400 million  
130 grid points with horizontal grid spacing of 2.5 km. The vertical grid has 144 stretched levels (Gal-Chen and  
131 Somerville, 1975) with a spacing of 250 m in the free troposphere and the stratosphere and a finer resolution  
132 of 100 m close to the surface and between 16 and 19.5 km inside the TTL. The simulation domain covers  
133 northern India and China (Fig. 1,  $5000 \text{ km} \times 3600 \text{ km}$ ) encompassing the track of flight #7 and the overshooting  
134 clouds over the Sichuan basin. The simulation was initialized at 00:00 UTC on 6 August 2017 and the initial  
135 and lateral boundary conditions are provided by the operational European Centre for Medium-Range Weather  
136 Forecasts (ECMWF) analyses every 6 hours. It ran for 3 days providing outputs every 1 hour.

137 The model employs a 1-moment bulk microphysical scheme (Pinty and Jabouille, 1998), which governs  
138 the equations of six water categories (water vapour, cloud water, rainwater, pristine ice, snow and graupel).  
139 For each particle type, the sizes follow a generalized Gamma distribution while power-law relationships allow  
140 the mass and fall speed to be linked to the diameters. Except for cloud droplets, each condensed water species  
141 has a nonzero fall speed. The turbulence parametrisation is based on a 1.5-order closure (Cuxart et al., 2000)  
142 of the turbulent kinetic energy equation and uses the Bougeault and Lacarrere (1989) mixing length. The  
143 transport scheme for momentum variables is the weighted essentially non-oscillatory (WENO) scheme of 5<sup>th</sup>  
144 order (Shu and Osher, 1988) while other variables are transported with the piecewise parabolic method (PPM)

145 scheme (Colella and Woodward, 1984).

146 To assess the simulation, airborne measurement data (along about 85.2°E, 25–26.5°N, blue line in Fig.  
147 1) between 06:20 and 06:48 UTC on 8 August 2017 are compared to the simulation results averaged in a box  
148 (85–85.5°E, 25–26.5°N, marked by ‘HYD’ in Fig. 1) at 06:00 UTC on the same day. The CALIOP backscatter  
149 coefficients are compared to those simulated from the model outputs using the Meso-NH lidar simulator, which  
150 takes into account all the predicted scattering particles (Chaboureau et al. 2011). The SEVIRI/MSG BTs are  
151 compared to synthetic BTs computed offline using the Radiative Transfer for TIROS Operational Vertical  
152 Sounder (RTTOV) code version 11.3 (Saunders et al. 2013) from the simulation outputs (Chaboureau et al.  
153 2008).

154 In this study, a ‘hydration patch’ is defined as a region with a water vapour amount larger than the  
155 background value at 410 K isentropic level. The background equals 5.2 ppmv which corresponds to the water  
156 vapour averaged in the box 74–84°E, 15–25°N (shown with dashed line in Fig. 1). Such a hydration patch is  
157 located within the moist layer (ML) of 18–19 km altitude (see Figure 2), corresponding to an enhanced value  
158 of water vapour observed during the last descending of flight #7 (see section 3.1). Below the hydration patch,  
159 the ice layer (IL) is located between 17 and 18 km, where an increase of ice content is observed during the  
160 same period. The hydration patch is chased visually back in time every hour from 06:00 UTC on 8 August to  
161 13:00 UTC on 6 August 2017, considering the prevailing wind direction and speed at 410 K isentropic altitude.  
162 At 14:00 UTC, a large amount of water vapour ( $\geq 6.6$  ppmv), that is injected by the convective overshoot in  
163 the Sichuan basin, starts to appear at this altitude, generating a hydration patch. With the dominant east-  
164 northeasterlies ( $15\text{--}20\text{ m s}^{-1}$ ), it travels to the south of Kathmandu. The area of the hydration patch is about  
165  $6,000\text{ km}^2$ , but it is reduced by one fourth to about  $1,500\text{ km}^2$  during the initial overshooting phase in the  
166 convective region. This domain is used to calculate the average values of water vapour, ice content,  
167 temperature, and relative humidity displayed in Figures 9, 10, and 11.

168 To understand the processes along the pathway of the hydration patch, four analysis times are selected:  
169 1) a few hours before the overshoot development at 13:00 UTC on 6 August, 2) the overshoot development  
170 time at 21:00 UTC on the same day, 3) a few hours after the overshoots at 12:00 UTC on 7 August, and 4) the  
171 aircraft measurement time at 06:00 UTC on 8 August 2017. There exist several tropopause definitions,  
172 considering temperature lapse rate, potential vorticity, and static stability (WMO, 1957; Maddox and  
173 Mullendore, 2018). In this study, the overshoots are defined as convective cloud tops that reach the lowermost

174 stratosphere above 380 K level. This simple definition is sufficient enough to study the impact of convective  
175 hydration on the TTL as it quickly returns to its undisturbed state (Dauhut et al., 2018). A tracer of tropospheric  
176 air is also calculated on line during the Meso-NH run. At the simulation initiation, the tropospheric and  
177 stratospheric air masses are divided by a boundary at 380 K level, and the tracer values are set to 1 and 0 below  
178 and above, respectively. In other words, pure concentration of tropospheric (stratospheric) air has tracer value  
179 equal to 100 (0) %.

180

### 181 **3. Convective hydration in the TTL**

#### 182 *3.1. Moistened layers in the TTL*

183 FISH and FLASH instruments on board flight #7 measure moisture and ice content in the TTL to the south of  
184 Kathmandu along the track of  $\sim 85.2^\circ\text{E}$ ,  $25\text{--}26.5^\circ\text{N}$  (blue line in Fig. 1) from 06:20 to 06:48 UTC on 8 August  
185 2017. ML and IL were observed. ML is evident at altitudes of 18–19 km by the water vapour content of 4.8–5.7  
186 ppmv (solid line in Fig. 2a), and IL is apparent at altitudes of 17–18 km with the ice content of up to 1.9 eq.  
187 ppmv (solid line in Fig. 2b) and water vapour of 3.3–5.0 ppmv (solid line in Fig. 2a). The temperature  
188 minimum, which defines the cold point tropopause (CPT, red line in Fig. 2c), equals  $-83.5^\circ\text{C}$  at 17.8 km in  
189 between ML and IL (black line in Fig. 2c). In ML, the potential temperature ranges between 394 and 428 K,  
190 while in IL it ranges between 372 and 393 K (blue line in Fig. 2c). Figure 2d shows that  $\text{RH}_{\text{ice}}$  increases beyond  
191 70 % in ML and IL, and that IL is partly super-saturated with  $\text{RH}_{\text{ice}}$  up to 118 %. In both ML and IL, strong  
192 easterly wind prevails (black line in Fig. 2e) with wind speed exceeding  $20\text{ m s}^{-1}$  (blue line in Fig. 2e), while  
193 easterlies stronger than  $30\text{ m s}^{-1}$  are seen at 17 and 18.5 km altitudes.

194 Figure 2 also evidences that Meso-NH succeeds in reproducing most of the measurements in the TTL.  
195 It reproduces the enhanced amount of water vapour in both ML and IL. In ML, the simulated water vapour in  
196 the range between 4.9–6.0 ppmv with an average value (black cross marks in Fig. 2a) of 5.5 ppmv reproduces  
197 the measured 4.2–5.6 ppmv well. In IL, the appearance of ice (black cross marks in Fig. 2b) is simulated, but  
198 with a maximum value of 0.65 eq. ppmv, a factor of 3 less compared to the measured concentrations. The  
199 simulation captures well the CPT at 17.8 km altitude and  $-83.3^\circ\text{C}$  (cross marks in Fig. 2c),  $\text{RH}_{\text{ice}}$  values of  
200 70–100 % between 16.5–18.5-km altitudes (cross marks in Fig. 2d), and the strong easterly wind (black and  
201 blue cross marks in Fig. 2e). Despite small vertical variations in water vapour and temperature that are missing

202 around the CPT, the simulation is good enough to being used to investigate the source and the pathways of  
203 water in ML and IL.

204 A few hours before the Geophysica measurements and upstream, some clouds were observed in the TTL  
205 by CALIOP around 20:00 UTC on 7 August 2017. Figure 3a shows a V-shaped region of strong backscatter  
206 values of  $0.001\text{--}0.008\text{ km}^{-1}\text{ sr}^{-1}$  from 15 to 18.5 km altitudes over India along the track of  $25.5\text{--}31.5^\circ\text{N}$  (yellow  
207 line in Fig. 1). The V-shaped strong backscatter region is successfully reproduced by Meso-NH (Fig. 3b) at  
208 15–18.5-km altitudes between  $26.5$  and  $31^\circ\text{N}$  but with backscatter values lower than measured. The simulated  
209 V-shaped region is characterized by low ice content ( $\geq 0.1$  eq. ppmv, Fig. 3c) while an above-background  
210 amount of water vapour of 5–7 ppmv is layered at altitudes higher than 18 km, (Fig. 3d), where ML is located.  
211 The V-shaped strong backscatter region is possibly induced by waves propagating at these high altitudes, e.g.  
212 gravity waves. Investigating the mechanism at its origin is however beyond the scope of this article. It is worth  
213 noting that the above-background water vapour concentration and the ice content are already upstream  
214 ( $93\text{--}95^\circ\text{E}$ ) about 10 hours before flight #7 ( $\sim 85.2^\circ\text{E}$ ) and that Meso-NH is able to resolve clouds in the UTLS.

215

### 216 *3.2. Target convective overshoots*

217 In the region where ML and IL are located, the simulated hydration patch (water vapour  $\geq 5.2$  ppmv) is in  
218 evidence at the 410 K level at 06:00 UTC on 8 August 2017 (Fig. 4a). It is positioned above high-level clouds,  
219 as shown with BT values lower than  $-47^\circ\text{C}$  in both the SEVIRI/MSG imagery and the Meso-NH simulation  
220 in Fig. 5a and 5b (pointed by arrows), respectively. This hydration patch has been advected from the east by  
221 the strong easterlies (about  $25\text{ m s}^{-1}$ , see Fig. 2e). At 12:00 UTC on 7 August, it is located around eastern India  
222 (Fig. 4c) and is associated with low BT values ( $\leq -55^\circ\text{C}$ ) in both the MSG/SEVIRI imagery (pointed by an  
223 arrow in Fig. 5c) and the Meso-NH simulation (Fig. 5d). This suggests that the hydration patch is generated  
224 by the injection of water by convective overshoots. The convective overshoots start to be seen from 14:00 UTC  
225 on 6 August over the Sichuan basin (Fig. 4e), and they overshoots develop in this region until 21:00 UTC.  
226 During the period between 14:00 and 21:00 UTC, the developing overshoots collectively inject a large water  
227 vapour hourly budget of 896 t above the CPT (as the result of integrating the water vapour content between  
228 two isentropic altitudes of 380 and 530 K). The signature of overshoots is evidenced over the Sichuan basin at  
229 21:00 UTC by the large amount of water vapour in excess of 18 ppmv at 410 K level (Fig. 4d) and by BT  
230 values lower than  $-80^\circ\text{C}$  (Fig. 5e and 5f). At 13:00 UTC before the overshoot development, neither water

231 vapour mixing ratio larger than 5 ppmv nor BT values lower than  $-60^{\circ}\text{C}$  are distinguishable over the Sichuan  
232 basin (box in Fig. 5g and 5h).

233 In summary, a good agreement is achieved between the measurements (airborne and spaceborne) and  
234 the Meso-NH simulation. The analysis of the simulation shows that the water-enhanced layers in ML and IL  
235 observed to the south of Kathmandu around 06:30 UTC on 8 August were generated by the injection of water  
236 by the convective overshoots produced over the Sichuan basin during 14:00–21:00 UTC on 6 August.

237

#### 238 **4. Pathway of the hydration patch and processes affecting it**

##### 239 *4.1. Evolution of the hydration patch during its way to the south of Kathmandu*

240 The hydration patch is described along its way from the Sichuan basin to the south of Kathmandu. In the  
241 following, vertical sections of water vapour, ice content and tropospheric tracer are shown across the hydration  
242 patch in the west-east orientation every 2 to 6 h (Figs. 6, 7, and 8). The vertical cross-sections are centred over  
243 the hydration patch, all with the same size.

##### 244 *4.1.1. Injection of water into the TTL by convective overshoots*

245 The vertical cross-sections of water vapour and ice content evidence that the large amounts of water vapour  
246 and ice are injected above 380 K level by the convective overshoots that occurred during 15:00–21:00 UTC  
247 on 6 August. At 13:00 UTC (Fig. 6a), just before the overshoot development, a strong upward motion is seen  
248 at 16–18-km altitudes, while the cloud top (black solid line) is located in IL (about 17.5 km), just below the  
249 CPT. At 15:00 UTC (Fig. 6b), a large amount of water vapour ( $\geq 15$  ppmv) is in evidence in ML above 410 K  
250 level while a large ice content in excess of 120 eq. ppmv is found in IL, between 380 and 410 K levels (Fig.  
251 7b). Figure 8a–b shows that during 15:00–17:00 UTC the concentration of the tropospheric tracer increases in  
252 both ML and IL with values of 4 and 30 %, respectively.

253 At 17:00 UTC and even higher cloud top is apparent at  $\sim 19.5$  km altitude (Fig. 6c), a large amount of  
254 water vapour ( $\geq 18$  ppmv) rises to  $\sim 20$  km, around  $103^{\circ}\text{E}$ , and a large ice content ( $\geq 120$  eq. ppmv) stays below  
255 18 km altitude (Fig. 7c). The large amount of water is directly injected by convective overshoots mainly in the  
256 form of ice, as the air within the overshooting of the ice-laden air mixes with the entrained stratospheric air  
257 during the collapse of the overshooting top. The warm, sub-saturated stratospheric air causes the ice to rapidly  
258 sublimate into water vapour at the top of the overshoot, moistening the layer. It is worth noting the water  
259 injected by the convective overshoots at 15:00 UTC is still apparent in ML at 17:00 UTC around  $102^{\circ}\text{E}$  with

260 a water vapour mixing ratio above 9 ppmv (Fig. 6c). In a similar way, the convectively-injected large moisture  
261 at 17:00 UTC around 103°E (Fig. 6c) is found in ML at 19:00 UTC around 102.5°E with a water vapour mixing  
262 ratio larger than 15 ppmv (Fig. 6d). At 19:00 UTC (Fig. 6d), the strong convective updraughts perturb the  
263 isentropic surfaces (red solid lines), descending the 410 K level largely from about 18.5 to 17.5 km. At 21:00  
264 UTC a higher cloud top is found above ML in a wide area (102.3–103.3°E longitude). The injected water  
265 vapour ( $\geq 18$  ppmv) is transported above 20.5 km (Fig. 6e) while the concentration of 0.1–0.5 % of the  
266 tropospheric tracer is seen in the water vapour pocket. The large ice content exceeding 120 eq. ppmv is  
267 distributed mostly in IL (Fig. 7e). During 15:00–21:00 UTC (Fig. 8b–e), a concentration of 2–20 % of the  
268 tropospheric tracer is consistently seen in ML, while higher concentration of 40 % has been found in IL. During  
269 17:00–21:00 UTC (Fig. 9c–e), the large turbulent kinetic energy (TKE) of 0.2–0.9  $\text{m}^2 \text{s}^{-2}$  is apparent in a  
270 limited area of cloud top ( $\sim 103^\circ\text{E}$ ).

#### 271 *4.1.2. Evolution of the hydration patch along its pathway*

272 From 23:00 UTC on 6 August to 06:00 UTC on 8 August 2017, the convective overshoots gradually diminish  
273 in the region of longitude  $\sim 98$ – $85^\circ\text{E}$  and latitude  $\sim 28$ – $25^\circ\text{N}$  (see Fig. 4). At 23:00 and 00:00 UTC, the anvil-  
274 shaped cloud above 16 km altitude presents a rather flat cloud top around 19 km (Fig. 7f and 7g). The injected  
275 large amount of water vapour  $\geq 18$  ppmv is evident in ML, even at higher altitudes up to 20.5 km (Fig. 6f and  
276 6g) whereas the large ice content  $\geq 120$  eq. ppmv is no longer apparent in IL (Fig. 7f and 7g). Within the anvil  
277 cloud, still large TKE of 0.2–0.9  $\text{m}^2 \text{s}^{-2}$  is seen (Fig. 9f, g). During 06:00–18:00 UTC on 7 August, the water  
278 vapour mixing ratio in ML gradually decreases from 15 to  $\sim 9$  ppmv, meanwhile the air mass in IL becomes  
279 dry with a water vapour mixing ratio below 4 ppmv (Fig. 6h–j). During the same period, the increase of  
280 tropospheric tracer concentration and TKE are evident in both ML and IL. The air mass with concentration  
281 higher than 40 % is apparent in IL while the air mass with a lower tropospheric concentration around 0.02–0.3  
282 is seen in IL (Fig. 8h–j).

283 The air mass with high tropospheric tracer concentration of 2–40 % consistently exists in ML and IL  
284 from 00:00 to 06:00 UTC on 8 August 2017 (Fig. 8k–l), while the TKE of 0.2–0.9  $\text{m}^2 \text{s}^{-2}$  exists in wide area  
285 between the altitudes of 16 and 18 km (Fig. 9k–l). During this period, the hydration patch is further narrowed  
286 and widened in ML (Fig. 6k–l), and the air mass becomes drier in IL ( $\leq 3$  ppmv). At 00:00 UTC (Fig. 7k), new  
287 convection tops are apparent in altitudes of 16–17 km, and an increase of ice content above 3 eq. ppmv is seen  
288 in IL. Then a decrease of ice content down to 0.1–1 eq. ppmv distributes in IL at 06:00 UTC where large ice

289 content around 1–1.9 eq. ppmv was measured (see Fig. 2b).

290

#### 291 *4.2. Processes affecting the hydration patch*

292 The processes that affect the moist and ice layers are further described. To this objective, average quantities  
293 are calculated in ML and IL. The hourly evolution of water vapour, ice content, temperature, and  $RH_{ice}$  shows  
294 the lifetime of the injected water in ML and IL along the pathway of the hydration patch (Fig. 10). The profiles  
295 of tropospheric tracer, temperature,  $RH_{ice}$ , water vapour, ice content and wind speed give a vertical view in the  
296 column across the tropical tropopause layer (Fig. 11). A scatter plot using tropospheric tracer and water vapour  
297 highlights the mixing processes occurring in the hydration patch (Fig. 12).

298

##### 299 *4.2.1. Mixing of the overshoots with the stratospheric air*

300 The hourly evolution of the average water vapour and the ice content along the pathway of the hydrated layer  
301 demonstrates the hydration in the TTL by the convective overshoots (Fig. 10). During the development of the  
302 convective overshoots between 14:00 and 21:00 UTC on 6 August 2017, the average water vapour mixing  
303 ratio increases to 5.7 ppmv in IL (yellow solid line, Fig. 10a), while a large mixing ratio of 6.5 ppmv is seen  
304 in ML (blue solid line in Fig. 10a). The ice content reaches more than 200 eq. ppmv in both layers and more  
305 than 300 eq. ppmv in IL (Fig. 10b). Until 17:00 UTC, the temperature increases in both layers (solid lines in  
306 Fig. 10c), indicating the mixing with the warmer stratospheric air. Because of this entrained stratospheric air,  
307  $RH_{ice}$  decreases largely below 60 % in ML (blue line with symbols in Fig. 10c), and down to 90 % in IL (yellow  
308 line with symbols). Due to the mixing with entrained warmer stratospheric air, the enriched water vapour layer  
309 then remains at this higher isentropic level after the overshoot collapses. The conditions and timescale of the  
310 detailed process trapping the enriched water vapour in the TTL was demonstrated by Dauhut et al. (2018).  
311 Thanks to a fine temporal resolution of 1 min, they revealed that this process occurs shortly within 20 min.  
312 The active mixing of the convective overshoots with the stratospheric air between 14:00 and 21:00 UTC is  
313 also evidenced by the evolution of vertical profiles of tropospheric tracer (Fig. 11a). The tropospheric tracer  
314 concentration increases from 0 to 5 % in ML (yellow to green lines in Fig. 11a), while the stratospheric air  
315 concentration (1 minus tracer) increases of 5 % in IL. The temperature increases in both ML and IL (yellow to  
316 green lines in Fig. 11b) where the relative humidity decreases (yellow to green lines in Fig. 11c).

317 The scatter plot of the tropospheric tracer and water vapour mixing ratio (Fig. 12) evidences the large

318 mixing of tropospheric and stratospheric air masses in the TTL (14–22 km altitudes). A large evolution of the  
319 tropospheric tracer–water vapour diagram is found from 13:00 to 21:00 UTC on 6 August (Fig. 12a and 12b).  
320 At 13:00 UTC before the development of the convective overshoots, the air mass with potential temperature  
321 ( $\theta$ ) of 410–420 K (yellow dots), corresponding to ML, is relatively dry with a water vapour mixing ratio of  
322 5–7.2 ppmv (Fig. 12a) and very small compounds of tropospheric air (tracer  $\leq 0.1$  %). The air mass with  $\theta$  of  
323 380–390 K (black dots), corresponding to IL, has a low water vapour mixing ratio of 3–7.5 ppmv. At 21:00  
324 UTC (Fig. 12b), the air mass with  $\theta$  between 410 and 420 K becomes very humid (5.5–13.6 ppmv of water  
325 vapour) and the concentration of tropospheric tracer increases to 0.2–8 %. Moreover the air mass with very-  
326 high  $\theta$  of 450–460 K (purple dots) is moistened largely as shown by a water vapour mixing ratio above 15  
327 ppmv. So does the air mass with  $\theta$  between 390 and 410 K, which is both moistened and enriched by the  
328 tropospheric tracer with a concentration of 5–60 % (red to orange dots, Fig. 12b). The convective overshoots  
329 also impact the air mass below the CPT by widening the range of the water vapour mixing ratio with  $\theta$  between  
330 370 and 380 K (grey dots in Fig. 12a and b) from 3.2–13.9 ppmv at 13:00 UTC (Fig. 12a) to 0–18.8 ppmv at  
331 21:00 UTC (Fig 12b).

332 From 17:00 UTC on 6 August to 02:00 UTC on 7 August, Fig. 9c shows that the temperature decreases  
333 gradually (solid lines), while the relative humidity increases (lines with symbols). In ML and IL, a great part  
334 of ice contents, especially snow and graupel fall quickly (dashed line in Fig. 10b), and the rest sublimates.  
335 Meanwhile ice sediment out, still there is a low concentration of cloud ice in both ML and IL, and the water  
336 vapour concentration slightly decreases (blue solid line in Fig. 10a). The continued presence of cloud ice in  
337 ML suggests that the ice may have formed in-situ in response to wave-driven temperature oscillations that  
338 locally drive the RH to ice saturation. The ice microphysics might play a pivotal role in controlling the eventual  
339 moisture content since ice nucleation and the subsequent growth process to deplete slowly the ML. In ML, the  
340 relative humidity increases (in range of 65–80 %) mainly due to the temperature decrease (in range of –78 and  
341 –82°C) (solid lines, Fig. 10c). During this period, the easterly wind is nearly constant with the relatively-weak  
342 speed of  $\sim 15$  m s<sup>-1</sup> in ML and  $\sim 16.5$  m s<sup>-1</sup> in IL (yellow to green lines, Fig. 11f). After 7 August, in ML, the  
343 relative humidity less than 80 % indicates strong sub-saturation where a very small amount (0.1–0.3 eq. ppmv)  
344 of cloud ice still resides. This is probably induced by the domain-averaged analysis.

345

346 *4.2.2. Processes occurring in the hydration patch during the advection*

347 After the development of the convective overshoots, the hydration patch travels westward across India and  
348 north Bangladesh from 21:00 UTC on 6 August to 06:00 UTC on 8 August (Fig. 4). During its travel, the air  
349 mass in ML and IL has less and less amount of water vapour and ice content (Fig. 10a–b).

350 Between 21:00 UTC on 6 August and 12:00 UTC on 7 August, the concentration of tropospheric tracer  
351 increases at high altitudes with  $\theta$  between 410 and 420 K up to 18 % (yellow dots, Fig. 12b–c). At the same  
352 time, the water vapour decreases by a factor of two, in the range of 5–9.6 ppmv. This can be also seen in the  
353 vertical profiles for which the concentration of tropospheric tracer increases at 12:00 UTC on 7 August in both  
354 ML and IL (green to blue lines, Fig. 11a) and the water vapour decreases (green to blue lines, Fig. 11d). The  
355 two layers become colder by  $\sim 3^\circ\text{C}$  (green to blue lines in Fig. 11b), and dehydrated compared to the initial  
356 state of 13:00 UTC on 6 August (yellow line in Fig. 11d, e). It includes much reduced amount of ice content  
357 (green to blue solid lines in Fig. 11e), but still there exist ice content  $\geq 1$  eq. ppmv and cloud ice  $\geq 0.5$  eq. ppmv  
358 at 12:00 UTC on 7 August (blue dashed line, Fig. 11e). In IL (Fig. 10c),  $\text{RH}_{\text{ice}}$  oscillates mostly driven by  
359 temperature variation. Over time, the air mass in ML and IL gets colder and less humid by the lowered cloud  
360 top below 17 km altitude. In both ML and IL, the easterly winds weaken below  $15 \text{ m s}^{-1}$ . Moreover, the  
361 turbulent kinetic energy (TKE) increases from  $0.1\text{--}0.3 \text{ m}^2 \text{ s}^{-2}$  at 21:00 UTC to  $0.2\text{--}0.9 \text{ m}^2 \text{ s}^{-2}$  at 12:00 UTC in  
362 ML and IL (Fig. 9e, i). These results suggest that the water vapour concentration in ML and IL decreases due  
363 to the turbulent diffusion in both the vertical and the horizontal direction consistent with the increase of  
364 tropospheric tracer. Also, the vapour-scavenging effect by ice nucleation and growth within IL contributes to  
365 reduce the water vapour deriving the dehydration. The rapid decrease of ice content in IL due to both  
366 sublimation and sedimentation (Fig. 7f–i) results in the lowering of the cloud top from 17 to below 16 km at  
367  $97\text{--}101^\circ\text{E}$  at 06:00 UTC (Fig. 7h), and finally to 15 km around  $95.5^\circ\text{E}$  at 12:00 UTC (Fig. 7i).

368 Further increased tropospheric tracer concentration is distinguished from 12:00 UTC on 7 August to  
369 06:00 UTC on 8 August 2017 in ML and IL (blue to red lines, Fig. 11a). Moreover the tropospheric tracer  
370 concentration reaches to about 30 and 70 % in ML and IL, respectively while the water vapour decreases (Fig.  
371 11a and 11d). During this time, the cloud top height of convective cloud descends below 14 km (Fig. 6i–l),  
372 where  $\text{RH}_{\text{ice}}$  dramatically decreases (Figs. 2d, 11c). The entrained cold tropospheric air (and/or colder  
373 background air) and the hydrostatic adjustment decrease the temperature in ML and IL (Fig. 11b). It is worth  
374 noting the shape of the temperature profile that becomes straight upward in the altitudes of 17–18.5 km during  
375 the overshoot activity (green line, Fig. 11b). Also it is worth noting the decrease of ice content less than 0.3

376 eq. ppmv (blue to red line, Fig. 11e), and the large-decrease of relative humidity in altitudes below 17.5 km.

377 The increased tropospheric tracer concentration in ML and IL is as well seen by the tracer–vapour  
378 diagram of Fig. 12c–d. The concentration of tropospheric tracer increases at high altitudes with  $\theta$  between 410  
379 and 420 K (yellow dots) up to 20 % at 06:00 UTC on 8 August 2017, meanwhile the tropospheric air  
380 concentration increases up to 50 % at the altitudes with  $\theta$  between 390 and 400 K (red dots in Fig. 12d). During  
381 the period (12:00 UTC on 7 August to 06:00 UTC on 8 August), the water vapour decreases in all altitudes  
382 with  $\theta$  above 380 K (Fig. 12c–d). It decreases from 9.6 to below 6.2 ppmv in ML ( $\theta$  between 410–430 K,  
383 yellow and green dots) while dropping below 5 ppmv in IL ( $\theta$  between 380–400 K, red and black dots). The  
384 reduced ice content in ML and IL might be induced by sedimentation thanks to the mixing with the dry  
385 tropospheric air ( $RH_{ice} \sim 50\text{--}70\%$ ) of below 16 km level (red line in Fig. 11c and cross marks in Fig. 2d). The  
386 air mixing of tropospheric and stratospheric air masses might be induced by the vertical wind shear with the  
387 maxima wind speeds in excess of  $30\text{ m s}^{-1}$  at  $\sim 17$  and  $18.5$  km altitudes (see Fig. 2e, average value in range of  
388  $18$  and  $25\text{ m s}^{-1}$  of red line in Fig. 11f). With the strengthened easterlies, the air mass in IL is well mixed rather  
389 than conserved in this layer. Also, this wind shear layer with a large gradient of wind speed ( $25\text{--}35\text{ m s}^{-1}$ )  
390 locates below and above the CPT (Fig. 2c, 2e), thus it results in the strait upward temperature profile with the  
391 constant value about  $-80^\circ\text{C}$  at 06:00 UTC on 8 August as seen in Fig. 10b (red line). The air mass in ML and  
392 IL has large TKE values of  $0.5\text{ m}^2\text{ s}^{-2}$  (Fig. 9l).

393

## 394 5. Conclusions

395 The source and pathway of the hydration patch in the TTL (Tropical Tropopause Layer) that was measured  
396 during flight #7 of the StratoClim 2017 field campaign during the Asian summer monsoon, and its connection  
397 to overshooting convection are investigated. During the Geophysica flight #7 around 06:30 UTC on 8 August  
398 2017, two remarkable layers were observed to the south of Kathmandu above and below the CPT located at  
399  $17.8$  km, a moist layer (ML) with large water vapour content of  $4.2\text{--}5.6$  ppmv in altitudes of  $18\text{--}19$  km in the  
400 lower stratosphere, and an ice layer (IL) with large ice content up to  $1.9$  eq. ppmv at altitudes of  $17\text{--}18$  km in  
401 the upper troposphere. The Meso-NH numerical simulation run with a  $2.5$  km horizontal grid spacing succeeds  
402 in reproducing ML and IL. Through analysis using airborne and spaceborne measurements and the numerical  
403 simulation, we show that the measured hydration patch in ML found in the south of Kathmandu ( $\sim 85^\circ\text{E}$ ) was  
404 produced by the convective overshoots that occurred over the Sichuan basin ( $\sim 103^\circ\text{E}$ ) between 14:00 and

405 21:00 UTC on 6 August 2017. The key hydration processes are summarized schematically in Fig. 13.

406 The convective overshoots develop up to 19.5 km altitude in the Sichuan basin, and transport large  
407 amount of water vapour of 6.5 ppmv to ML and ice content in excess of 300 eq. ppmv to IL. Between 15:00  
408 and 21:00 UTC, the overshooting clouds collectively hydrate the lower stratosphere resulting in the total  
409 amount of water vapour of 6088 t. It is also worth noting the large concentration of water vapour of over 18  
410 ppmv up to 20 km level which is above the convective cloud top of 19.5 km (a yellow ellipsoid in Fig. 13a).  
411 This feature is similarly seen during the development of the Hector the Convectoid in the Tiwi Islands (Dauhut  
412 et al., 2018), however, the magnitude is  $\sim 10$  ppmv higher in the present event. The concentration of the  
413 tropospheric tracer reaches to 8 and  $\sim 60$  % in ML and IL, respectively, indicating the strong mixing of the  
414 convective updraughts with the stratospheric air (black arrows in Fig. 13a). The strong convective updraughts  
415 perturb the isentropic surfaces (red line in Fig. 13a), descending the 410 K level from 18.5 to 17.5 km. During  
416 these convective events, the mixing of the tropospheric and stratospheric air masses increases the temperature  
417 in ML and IL. Moreover, the moderate -not intense- easterly wind ( $\sim 15$  m s<sup>-1</sup>) prevails constantly in these  
418 levels, and it does not interrupt the convection developing vigorously in altitude (19.5 km ASL) and reaching  
419 the lower stratosphere.

420 The injected water by the convective overshoots generates the hydration patch, i.e. large water vapour  
421 in ML (ellipse in Fig. 13b). During its westward travel, its altitude is kept constant by the moderate easterlies  
422 of about 15 ms<sup>-1</sup> in ML and IL. The tropospheric tracer concentration is continuously increased in these layers,  
423 where the above-background amount of water vapour is still remained and where the ice content gradually  
424 sediments out and forms again along the pathway. It is highlighted that the large transported amount of water  
425 vapour ( $\geq 18$  ppmv) still remains at high altitudes of up to 20.5 km even when the anvil cloud top descends to  
426 18.5 km. Later on, the cloud top is still seen around 16–17 km level, keeping the large RH<sub>ice</sub> (about 95 %) in  
427 these altitudes. A part of the water vapour has been lost due to ice formation and sedimentation and the  
428 turbulent diffusion in both vertical and the horizontal direction (black arrows in Fig. 13b). The ice microphysics  
429 might play a pivotal role in controlling the eventual moisture content since ice nucleation and the subsequent  
430 growth process would slowly deplete the water vapour. This falling of ice and a reduced updraught are evident  
431 by the lowered cloud top height partly from 17 to  $\sim 15$  km (Fig. 13c).

432 Then the hydration patch continues to travel to the south of Kathmandu, with even higher tropospheric  
433 tracer concentration of  $\sim 30$  and 70 % in ML and IL, respectively (darkened blue shades in Fig. 13c). During

434 the same period, the top of convective clouds further descends below 14 km, thus the layer below IL, i.e. 15–17  
435 km, becomes dry with  $RH_{ice}$  below 70 %. Due to mixing with the dry tropospheric air, the remaining water  
436 vapour in ML gradually diffused in horizontal and vertical direction (ellipse). It is also true that the ice content  
437 in IL is locally influenced by new convection with cloud top in altitudes 16–17 km about 6 h before flight #7.  
438 The continuous air mixing might be induced by the vertical wind shear in altitudes 15–19 km where the wind  
439 speed varies from  $\sim 18$  to  $25 \text{ m s}^{-1}$  (red bold arrows in Fig. 13c). The vertical mixing due to wind shear modifies  
440 the temperature profile to the straight-upward in 17–18 km rather than bending. Also, vertical motions caused  
441 by gravity waves breaking might play an important role in the transport of tropospheric air into the TTL. In  
442 addition, after the strong updraughts of overshooting convection, the remained horizontal divergence in the  
443 lower stratosphere might let the tropospheric air continues to ascend.

444 Many of previous Lagrangian studies (Tzella and Legras, 2011; Tissier and Legras, 2016) demonstrated  
445 the link between the moistened TTL and remote overshoots using large-scale numerical simulations. Thanks  
446 to the combination of aircraft measurement and a 3-day convection-permitting simulation, this study shed light  
447 on the processes along the pathway of a hydration patch from overshooting clouds for 1.5 days, showing the  
448 3-D evolution of water vapour and ice content.

449 This study focuses on the hydration patch that was measured during the last descending of flight #7 and  
450 the corresponding convective overshoots over the Sichuan basin. Here, the average water vapour amount in  
451 the lower stratosphere is 6.5 ppmv during the convective event while a water vapour of 6 ppmv is found above  
452 West Africa during the monsoon season by Khaykin et al. (2009). By comparison, convection developing  
453 during the Asian monsoon over the Sichuan basin had a similar impact on the stratospheric water budget as  
454 above West Africa. From the hourly budget of 869 t, we can also confirm that the local impact of overshoots  
455 developed during the Asian summer monsoon is stronger than the one over tropical Africa (300–500 t  
456 according to Liu et al., 2010) and is weaker than Hector the Convecton over the Tiwi Islands (2776 t according  
457 to Dauhut et al., 2015). Because of a large variety in the lifetime and horizontal scale of overshoots, an  
458 accumulation of more event-scale analyses is important. In addition, note that the amount of injected moisture  
459 is sensitive to the grid spacing of simulation and the convection duration of target system. The simple set up  
460 of tropospheric tracer of this study, i.e. tropospheric air below the 380 K isentropic altitude, allows to  
461 understand the mixture of tropospheric and stratospheric air parcels in the TTL by vigorous convective  
462 overshoots. To estimate the detailed origin i.e. defining the lower, middle, and upper troposphere, of air parcel,

463 further sophisticated analyses (e.g. Mullendore et al., 2005; Hassim and Lane, 2010; Homeyer, 2015; Dauhut  
464 et al., 2016) will be required. Also, additional numerical simulation with a 2-moment microphysical scheme  
465 that considers mass and number concentration of hydrometeors and aerosol together with options in the  
466 turbulent scheme (e.g., 1D against 3D formulation, Marchado and Chaboureau, 2015) will be worthwhile to  
467 study the impact on the results. To understand how much water vapour and ice are generally injected into the  
468 TTL through convective overshoots during the Asian summer monsoon is currently investigated in a follow-  
469 up study. Further, it would be interesting to investigate the transport of chemical constituents, e.g. methane,  
470 nitrogen oxides, and carbon monoxide, via convective overshoots during this season.

471

#### 472 **Author contribution**

473 KOL, TD and JPC designed the numerical simulation, and JPC performed the simulation. KOL, TD and JPC  
474 designed the manuscript and analyses. SK provided the FLASH instrument data, and MK and CR provided  
475 the FISH instrument data. KOL prepared the manuscript with contributions from all co-authors.

476

#### 477 **Acknowledgement**

478 This study is funded by the StratoClim project by the European Union Seventh Framework Programme under  
479 grant agreement no 603557 and the Idex TEASAO project. Computer resources were allocated by GENCI  
480 through project 90569.

481

#### 482 **References**

- 483 Afchine, A., Rolf, C., Costa, A., Spelten, N., Riese, M., Buchholz, B., Ebert, V., Heller, R., Kaufmann, S.,  
484 Minikin, A., Voigt, C., Zöger, M., Smith, J., Lawson, P., Lykov, A., Khaykin, S., and Krämer, M.: Ice  
485 particle sampling from aircraft – influence of the probing position on the ice water content, *Atmos.*  
486 *Meas. Tech.*, 11, 4015-4031, <https://doi.org/10.5194/amt-11-4015-2018>, 2018.
- 487 Bougeault, P. and Lacarrère, P.: Parameterization of orography-induced turbulence in a meso-beta-scale model.  
488 *Mon. Weather Rev.* 117(8): 1872–1890, 1989.
- 489 Chaboureau, J.-P., Cammas, J.-P., Duron, J., Mascart, P. J., Sitnikov, N. M., and Voessing, H. J.: A numerical  
490 study of tropical cross-tropopause transport by convective overshoots, *Atmos. Chem. Phys.*, 7, 1731–  
491 1740, 2007.

492 Chaboureau, J.-P., and Coauthors: A midlatitude precipitating cloud database validated with satellite  
493 observations. *J. Appl. Meteor. Climatol.*, 47, 1337–1353, [doi.org/10.1175/2007JAMC1731.1](https://doi.org/10.1175/2007JAMC1731.1), 2008.

494 Chaboureau, J.-P., and Coauthors: Long-range transport of Saharan dust and its radiative impact on  
495 precipitation forecast: A case study during the Convective and Orographically-induced Precipitation  
496 Study (COPS). *Quart. J. Roy. Meteor. Soc.*, 137, 236–251, [doi.org/10.1002/qj.719](https://doi.org/10.1002/qj.719), 2011.

497 Colella, P. and Woodward, P. R.: The piecewise parabolic method (PPM) for gas dynamical simulations. *J.*  
498 *Comput. Phys.* 54: 174–201, doi:10.1016/0021-9991(84)90143-8, 1984.

499 Cuxart, J., Bougeault, P., and Redelsperger, J. L.: A turbulence scheme allowing for mesoscale and large-eddy  
500 simulations. *Q. J. R. Meteorol. Soc.* 126(562): 1–30, doi: 10.1002/qj.49712656202, 2000.

501 Dauhut, T., Chaboureau, J. P., Escobar, J., and Mascart, P.: Large-eddy simulations of hector the convector  
502 making the stratosphere wetter. *Atmos. Sci. Let.* 16, 135–140, doi:10.1002/asl2.534. 2015.

503 Dauhut, T., Chaboureau, J. P., Haynes, P. H., and Lane, T. P: The mechanisms leading to a stratospheric  
504 hydration by overshooting convection. Accepted to *J. Atmos. Sci.*, 2018.

505 Dessler, A. E. and Sherwood, S. C.: Effect of convection on the summertime extratropical lower stratosphere,  
506 *J. Geophys. Res.*, 109, D23301, doi:10.1029/2004JD005209, 2004.

507 Fueglistaler, S., Dessler, A. E., Dunkerton, T. J., Folkins, I., Fu, Q., and Mote, P. W.: Tropical tropopause layer,  
508 *Rev. Geophys.*, 47, RG1004, doi:10.1029/2008RG000267, 2009.

509 Funatsu, B. M., Rysman, J. F., Claud, C., and Chaboureau, J. P.: Deep convective clouds distribution over the  
510 Mediterranean region from AMSU-B/MHS observations, *Atmos. Res.*, 207, 122-135,  
511 <https://doi.org/10.1016/j.atmosres.2018.03.003>, 2018.

512 Gal-Chen, T. and Somerville, R. C. J.: On the use of a coordinate transformation for the solution of the Navier-  
513 Stokes equations. *J. Comput. Phys.* 17: 209–228, doi:10.1016/0021-9991(75)90037-6, 1975.

514 Homeyer, C. R., Pan, L. L., Dorsi, S. W., Avallone, L. M., Weinheimer, A. J., O'Brien, A. S., DiGangi, J. P.,  
515 Zondlo, M. A., Ryerson, T. B., Diskin, G. S., and Campos, T. L.: Convective transport of water vapor  
516 into the lower stratosphere observed during double-tropopause events. *J. Geophys. Res. Atmos.*, 119,  
517 10941–10958, doi:10.1002/2014JD021485, 2014.

518 Homeyer, C. R.: Numerical simulations of extratropical tropopause penetrating convection, *J. Geophys. Res.*  
519 *Atmos.*, 120, 7174–7188. doi: 10.1002/2015JD023356, 2015.

520 Homeyer, C. R., McAuliffe, J. D., and Bedka, K. M.: On the development of above-anvil cirrus plumes in

521 Extratropical convection. *J. Atmos. Sci.*, 74, 1617–1633, <https://doi.org/10.1175/JAS-D-16-0269.1>,  
522 2017

523 Hassim, M. E. E. and Lane, T. P.: A model study on the influence of overshooting convection on TTL water  
524 vapour, *Atmos. Chem. Phys.*, 10, 9833–9849, <https://doi.org/10.5149/acp-10-9833-2010>, 2010.

525 Highwood, E. J., and Hoskins, B. J.: The tropical tropopause, *Q. J. R. Meteorol. Soc.*, 124, 1579–1604, 1998.

526 Hoskins, B. J. and Rodwell, M. J.: A model of the Asian summer monsoon, I, The global scale, *J. Atmos. Sci.*,  
527 52, 1329–1340, 1995.

528 Jensen, E., Ackerman, A. S. and Smith, J. A.: Can overshooting convection dehydrate the tropical tropopause  
529 layer? *J. Geophys. Res.*, 112, D11209, doi:10.1029/2006JD007943, 2007.

530 Kato T.: Structure of the band-shaped precipitation system inducing the heavy rainfall observed over northern  
531 Kyushu, Japan on 29 June 1999. *J. Meteor. Soc. Japan.* 84,129–153, 2006.

532 Khaykin, S. M., Pommereau, J.-P., Riviere, E. D., Held, G., Ploeger, F., Gysels, M., Amarouches, N., Vernier,  
533 J.-P., Wienhold, F. G., and Ionov, D.: Evidence of horizontal and vertical transport of water in the  
534 southern hemisphere tropical tropopause layer (TTL) from high-resolution balloon observation, *Atmos.*  
535 *Chem. Phys.*, 16, 12273–12286, 2016.

536 Khaykin, S., Pommereau, J.-P., Korshunov, L., Yushkov, V., Nielsen, J., Larsen, N., Christense, T., Garnier, A.,  
537 Lukyanov, A., and Williams, E.: Hydration of the lower stratosphere by ice crystal geysers over land  
538 convective systems, 9, 2275–2287, 2009.

539 Khaykin, S. M., Engel, I., Vömel, H., Formanyuk, I. M., Kivi, R., Korshunov, L. I., Krämer, M., Lykov, A. D.,  
540 Meier, S., Naebert, T., Pitts, M. C., Santee, M. L., Spelten, N., Wienhold, F. G., Yushkov, V. A., and  
541 Peter, T.: Arctic stratospheric dehydration – Part 1: Unprecedented observation of vertical redistribution  
542 of water, *Atmos. Chem. Phys.*, 13, 11503–11517, <https://doi.org/10.5194/acp-13-11503-2013>, 2013.

543 Lac, C., Chaboureaud, J. P., Masson, V., Pinty, J. P., Tulet, P., Escobar, J., Leriche, M., Barthe, C., Aouizerats,  
544 B., Augros, C., Aumond, P., Auguste, F., Bechtold, P., Berthet, S., Bieilli, S., Bosseur, F., Caumont, O.,  
545 Cohard, J. M., Colin, J., Couvreur, F., Cuxart, J., Delautier, J., Dauhut, T., Ducrocq, V., Filippi, J.B.,  
546 Gazen, D., Geoffroy, O., Gheusi, F., Honnert, R., Lafore, J. P., Lebeaupin, Brossier C., Libois, Q., Lunet,  
547 T., Mari, C., Maric, T., Mascart, P., Mogé, M., Molinié, G., Nuissier, O., Pantillon, F., Peyrillé, P.,  
548 Pergaud, J., Perraud, E., Pianezze, J., Redelsperger, J. L., Ricard, D., Richard, E., Riette, S., Rodier, Q.,  
549 Schoetter, R., Seyfried, L., Stein, J., Suhre, K., Taufour, M., Thouron, O., Turner, S., Verrelle, S., Vié,

550 B., Visentin, F., Vionnet, V., and Wautelet, P.: Overview of the Meso-NH model version 5.4 and its  
551 applications. *Geosci. Model Dev.*, 11, 1929–1969, 2018.

552 Liu, C., and Zipser, E. J.: Global distribution of convection penetrating the tropical tropopause, *J. Geophys.*  
553 *Res.*, 110, D23104, doi:10.1029/2005JD006063, 2005.

554 Machado, L. A., and Chaboureaud, J. P.: Effect of Turbulence Parameterization on Assessment of Cloud  
555 Organization. *Mon. Wea. Rev.*, 143, 3246–3262, <https://doi.org/10.1175/MWR-D-14-00393.1>, 2015.

556 Masson, V., Le Moigne, P., Martin, E., Faroux, S., Alias, A., Alkama, R., Belamari, S., Bardu, A., Boone, A.,  
557 Bouyssel, F., Brousseau, P., Brun, E., Calvet, J.C., Carrer, D., Decharme, B., Delire, C., Donier, S.,  
558 Essaouini, K., Gibelin, A. L., Giordani, H., Habets, F., Jidane, M., Kerdraon, G., Kourzeneva, E.,  
559 Lafaysse, M., Lafont, S., Lebeaupin, B.C., Lemonsu, A., Mahfouf, J.F., Marguinaud, P., Mokhtari, M.,  
560 Morin, S., Pigeon, G., Salgado, R., Seity, Y., Taillefer, F., Tanguy, G., Tulet, P., Vincendon, B., Vionnet,  
561 V., and Voldoire, A.: The surfex v7.2 land and ocean surface platform for coupled or offline simulation  
562 of earth surface variables and fluxes. *Geosci. Model Dev.* 6(4): 929–960, doi:10.5194/gmd-6-929-2013,  
563 2013.

564 Mason, R. and Anderson, C.: The development and decay of the 100-MB. Summertime anticyclone over  
565 southern Asia. *Mon. Wea. Rev.*, 1, 3–12, 1963.

566 Meyer, J., Rolf, C., Schiller, C., Rohs, S., Spelten, N., Afchine, A., Zöger, M., Sitnikov, N., Thornberry, T. D.,  
567 Rollins, A. W., Bozóki, Z., Tótrai, D., Ebert, V., Kühnreich, B., Mackrodt, P., Möhler, O., Saathoff, H.,  
568 Rosenlof, K. H., and Krämer, M.: Two decades of water vapor measurements with the FISH fluorescence  
569 hygrometer: a review, *Atmos. Chem. Phys.*, 15, 8521–8538, <https://doi.org/10.5194/acp-15-8521-2015>,  
570 2015.

571 Mullendore, G. L., Durran, D. R., and Holton, J. R.: Cross-Tropopause tracer transport in midlatitude  
572 convection, *J. Geophys. Res.*, 110, D06113, doi:10.1029/2004JD005059, 2005.

573 Park, M., Randel, W. J., Kinnison, E. J., Garcia, R. R., and Choi, W.: Seasonal variation of methane, water  
574 vapor and nitrogen oxides near the tropopause: Satellite observations and model simulation, *J. Geophys.*  
575 *Res.*, 109, D03302, doi:10.1029/2003JD003706, 2004.

576 Pinty, J. P. and Jabouille, P.: A mixed-phased cloud parametrization for use in a mesoscale non-hydrostatic  
577 model: Simulations of a squall line and of orographic precipitation. In: *Proc. Of the Conference on Cloud*  
578 *Physics. Amer. Meteorol. Soc, Boston: Everett, WA, USA, 17–21 Aug. 1998. Pp. 217–220, 1998.*

579 Randel, W. J. and Park, M.: Deep convective influence on the Asian summer monsoon anticyclone and  
580 associated tracer variability observed with Atmospheric Infrared Sounder (AIRS), *J. Geophys. Res.*, 111,  
581 D12314, doi:10.1029/2005JD006490, 2006.

582 Randel, W. J., Wu, F., Gettelman, A., Russell, J. M., Zawodny, J. M., and Oltmans, S. J.: Seasonal variation of  
583 water vapour in the lower stratosphere observed in Halogen Occultation Experiment data, *J. Geophys.*  
584 *Res.*, 106(D13), 14313–14325, 2001.

585 Rysman, J. F., Claud, C., Chaboureau, J. P., Delanoë, J., and Funatsu, B. M.: Severe convection in the  
586 Mediterranean from microwave observations and a convection-permitting model, *Quart. J. Roy. Meteor.*  
587 *Soc.*, 142, 43-55, <https://doi.org/10.1002/qj.2611>, 2016.

588 Rolf, C., Vogel, B., Hoor, P., Afchine, A., Günther, G., Krämer, M., Müller, R., Müller, S., Spelten, N., and  
589 Riese, M.: Water vapor increase in the lower stratosphere of the northern hemisphere due to the Asian  
590 monsoon anticyclone observed during the TACTS/ESMVal campaigns, *Atmos. Chem. Phys.*, 18,  
591 2973–2983, <http://doi.org/10.5194/acp-18-2973-2018>, 2018.

592 Saunders, R., Hocking, J., Rundle, D., Rayer, P., Matricardi, M., Geer, A., Lupu, C., Brunel, P., and Vidot, J.:  
593 RTTOV-11—Science and validation report. NWP SAF Tech. Rep., 62 pp., 2013.

594 Shu, C. W. and Osher, S.: Efficient implementation of essentially non-oscillatory shock-capturing schemes.  
595 *Journal of Computational Physics* 77(2): 439–471, 1988.

596 Sitnikov, N. M., Yushkov, V. A., Afchine, A. A., Korshunov, L. I., Astakhov, V. I., Elanovskii, A. E., Kraemer,  
597 M., Mangold, A., Schiller, C., and Ravegnani, F.: The FLASH instrument for water vapor measurements  
598 on board the high-altitude airplane. *Instrum. Exp. Tech.*, 50, 113–121, 2007.

599 Smith, J. B., Wilmouth, D. M., Bedka, K. M., Bowman, K. P., Homeyer, C. R., Dykema, J. A., Sargent, M. R.,  
600 Clapp, C. E., Leroy, S. S., Sayres, D. S., Dean-Day, J. M., Bui, T. P., and Anderson, J. G.: A case study  
601 of convectively sourced water vapor observed in the overworld stratosphere over the United States. *J.*  
602 *Geophys. Res.*, 122, 9529–9554, doi:10.1002/2017JD026831, 2017.

603 Tissier, A.-S. and Legras, B.: Convective sources of trajectories traversing the tropical tropopause layer. *Atmos.*  
604 *Chem. Phys.*, 16, 3383–3398, 2016.

605 Tzella, A. and Legras, B.: A Lagrangian particle dispersion model FLEXPART version 6.2. *Atmos. Chem.*  
606 *Phys.*, 5, 2461–2474, doi:10.5194/acp-5-2461-2005, 2005.

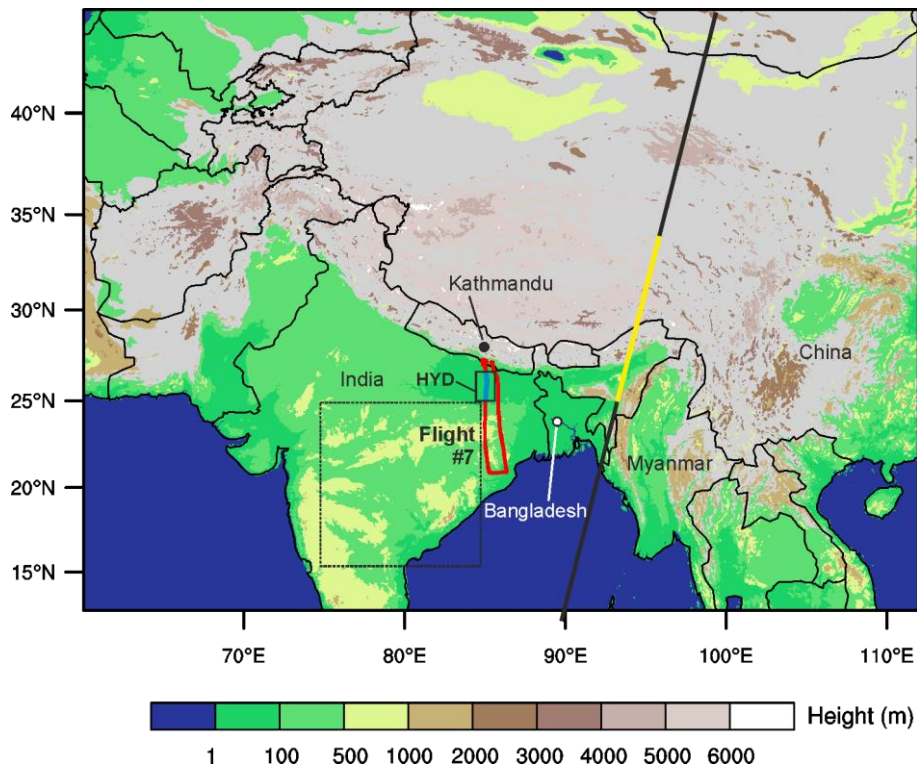
607 Winker, D. M., Vaughan, M. A., Omar, A., Hu, Y., Powell, K. A., Liu, Z., Hunt, W. H., and Young, S. A.:

608 Overview of the CALIPSO mission and CALIOP data processing algorithms. *J. Atmos. Oceanic*  
609 *Technol.*, 26, 2310–2323, [doi:10.1175/2009JTECHA1281.1](https://doi.org/10.1175/2009JTECHA1281.1), 2009.

610 Wright, J. S., Fu, R., Fueglistaler, S., Liu, Y. S., and Zhang, Y.: The influence of summertime convection over  
611 Southeast Asia on water vapor in the tropical stratosphere. *J. Geophys. Res.*, 116, D12302,  
612 [doi:10.1029/2010JD015416](https://doi.org/10.1029/2010JD015416), 2011.

613 Zöger, M., Afchine, A., Eicke, N., Gerhards, M.-T., Klein, E., McKenna, D., Mörschel, U., Schmidt, U., Tan,  
614 V., Tuitjer, F., Woyke, T., and Schiller, C.: Fast in situ stratospheric hygrometers: A new family of  
615 balloon-borne and airborne Lyman-photofragment fluorescence hygrometers, *J. Geophys. Res.*, 104,  
616 1807–1816, 1999.

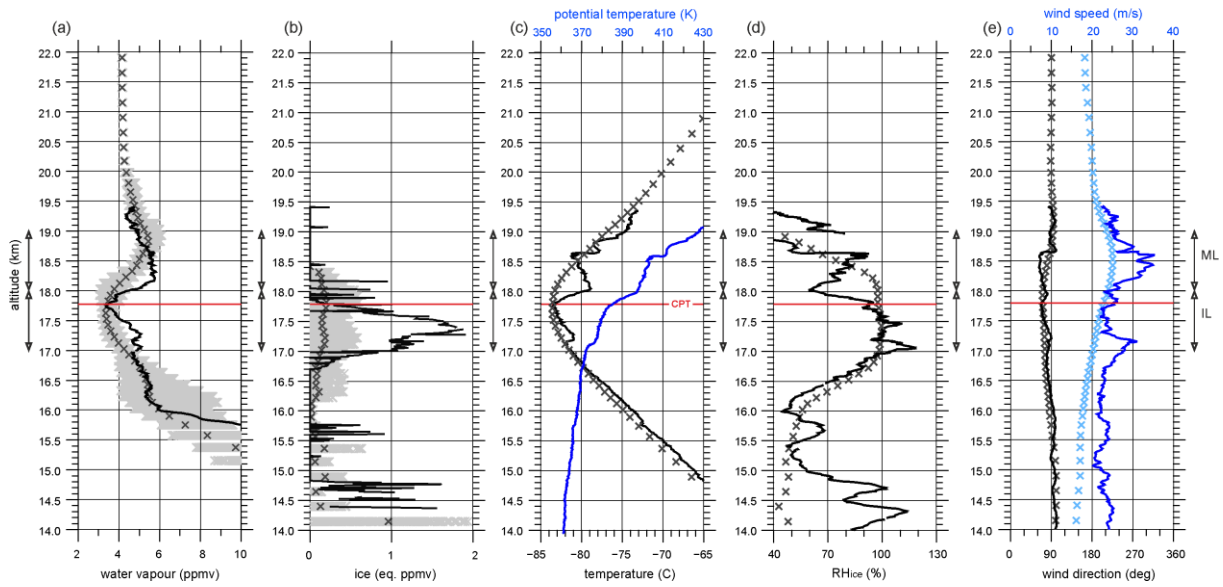
617



618

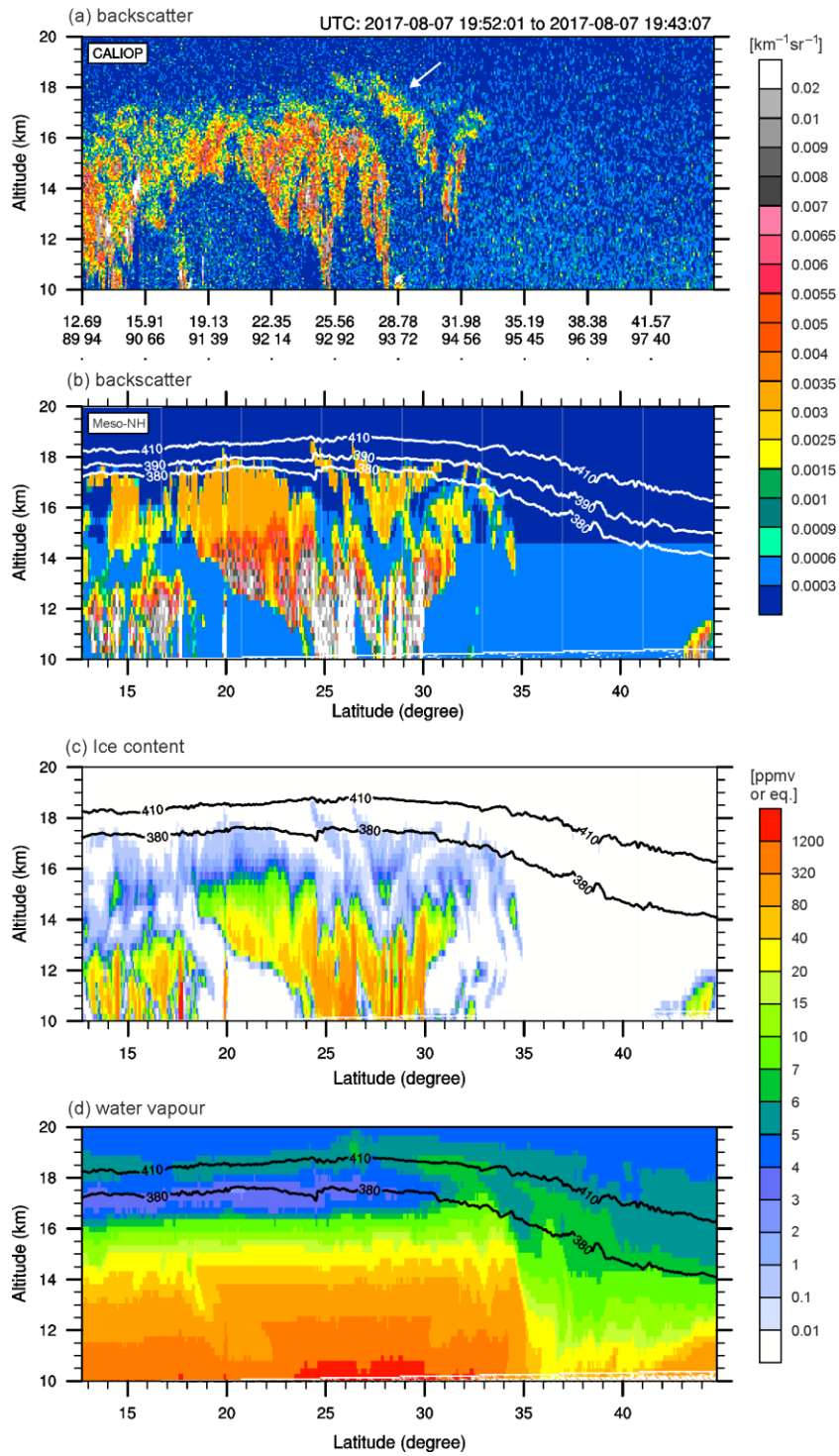
619 **Figure 1.** Topography and domain considered in the Meso-NH numerical simulation with a resolution of 2.5 km. The trajectory of the  
 620 Geophysica flight #7 to the south of Kathmandu is shown by the red solid line, while the pathway of moist patch (25–26.5°N) is  
 621 depicted by the blue line. A black box ‘HYD’ is a model domain considered in comparison with aircraft measurement. Another box  
 622 with dashed line is a model domain used to calculate the background water vapour at 06:00 UTC on 8 August 2017. The track of  
 623 CALIOP around 20:00 UTC on 7 August 2017 is shown by the black solid line while its track between 25 and 33°N is highlighted in  
 624 yellow.

625



626

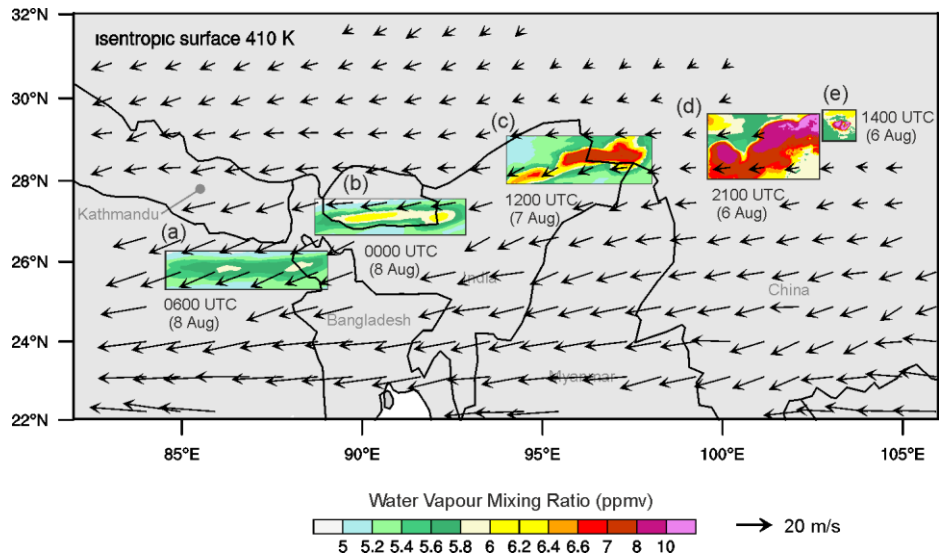
627 **Figure 2.** Vertical profiles of (a) water vapour (ppmv), (b) ice (eq. ppmv), (c) temperature ( $^{\circ}\text{C}$ ) and potential temperature (K), (d)  
 628 relative humidity respect to ice ( $\text{RH}_{\text{ice}}$ , %), and (e) wind direction (degree) and speed ( $\text{m s}^{-1}$ ). In (a)–(e), the measured values along the  
 629 blue-coloured track between  $25\text{--}26.5^{\circ}\text{N}$  (shown in Fig. 1) from 06:20 to 06:48 UTC on 8 August 2017 are shown as solid line, while  
 630 the domain averaged values in the region ‘HYD’ ( $25\text{--}26.5^{\circ}\text{N}$ ,  $85\text{--}85.5^{\circ}\text{E}$ , shown in Fig. 1) from the Meso-NH simulation at 06:00  
 631 UTC on the same day are shown as cross marks. In (a)–(e), the level of cold point tropopause (CPT) is indicated by a red line. In  
 632 (a)–(b), all the values from Meso-NH within the ‘HYD’ is displayed by grey cross marks. The layers of ML and IL are marked by  
 633 arrows.



634

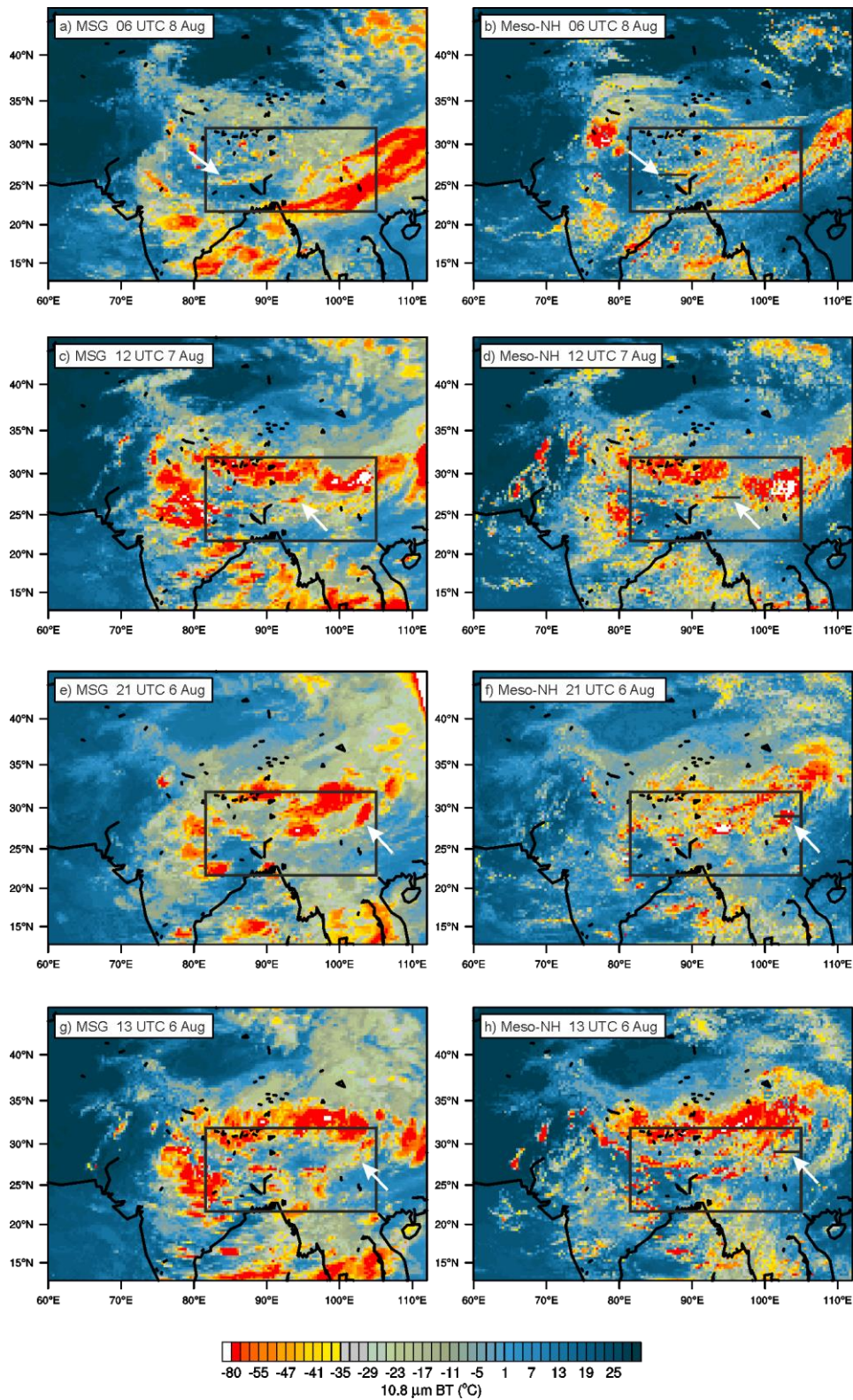
635 **Figure 3.** Backscatters at 532 nm (a) measured by CALIOP around 20:00 UTC and (b) retrieved by the Meso-NH simulation, and (c)  
 636 ice content (eq. ppmv) and (d) water vapour (ppmv) produced by the Meso-NH simulation along the CALIOP track (marked by solid  
 637 line in Fig. 1) at 20:00 UTC on 7 August 2017.

638



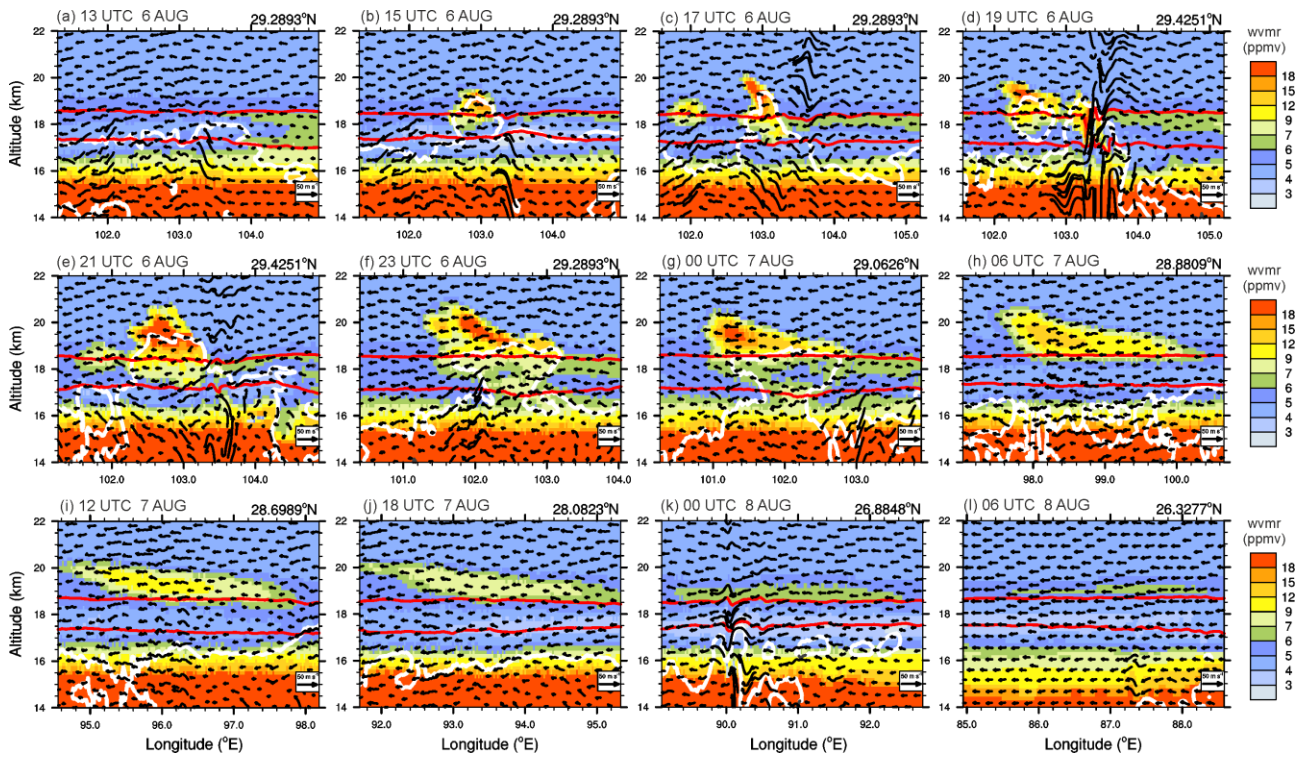
639

640 **Figure 4.** Target moist patch. Horizontal distribution of water vapour mixing ratio at 410 K isentropic altitude at (a) 06:00 UTC, and  
 641 (b) 00:00 UTC on 8 August, (c) 12:00 UTC on 7 August, (d) 21:00 UTC and (e) 14:00 UTC on 6 August 2017. The horizontal wind at  
 642 the altitude of 19 km (about 410 K isentropes) at 06:00 UTC on 8 August is displayed by vectors.



643

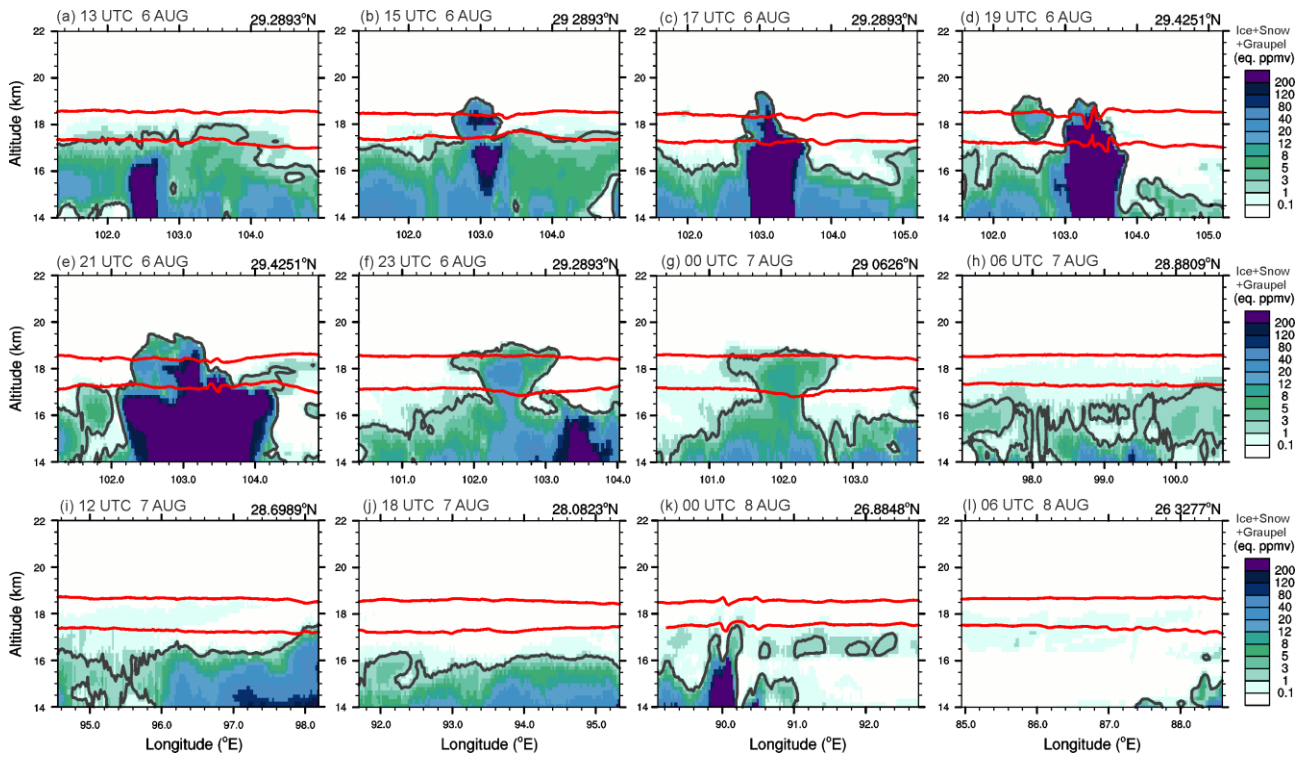
644 **Figure 5.** BT 10.8  $\mu\text{m}$  obtained from SEVIRI/MSG (left) and Meso-NH (right) at (a)–(b) 06:00 UTC on 8 August, (c)–(d) 12:00 UTC  
 645 on 7 August, (e)–(f) 21:00 UTC, and (f)–(h) 13:00 UTC on 6 August 2017. The domain used in Figure 4 is marked by a box in each  
 646 panel, while the location of vertical cross-sections used in Figures 6–9 is marked by a black solid line in the right panels. The location  
 647 of hydration patch is depicted by the white arrows.



648  
649

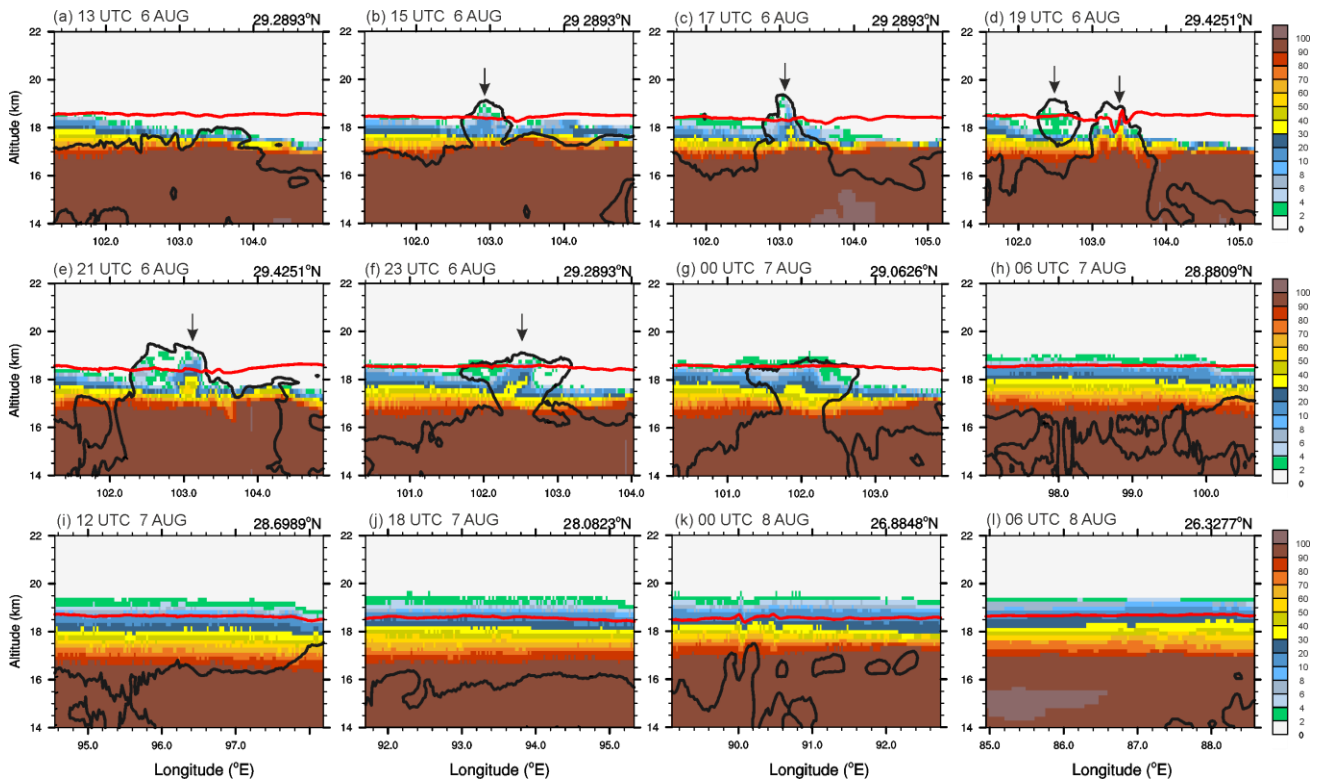
650 **Figure 6.** Vertical cross-sections of water vapour mixing ratio (shading) and wind (vectors) (a) 13:00 UTC, (b) 15:00 UTC, (c) 17:00  
651 UTC, (d) 19:00 UTC, (e) 21:00 UTC, (f) 23:00 UTC on 6 August 2017, (g) 00:00 UTC, (h) 06:00 UTC, (i) 12:00 UTC, (j) 18:00  
652 UTC on 7 August 2017, and (k) 00:00 UTC and (l) 06:00 UTC on 8 August 2017. The isentropic altitudes of 380 and 410 K are  
653 depicted by the red lines. The latitude ( $^{\circ}$ N) of west-east oriented cross-section line is indicated at the upper right of each panel. The  
654 cloud boundary (mixing ratio of ice content of  $10 \text{ mg kg}^{-1}$ ) is contoured by the white solid line.

655



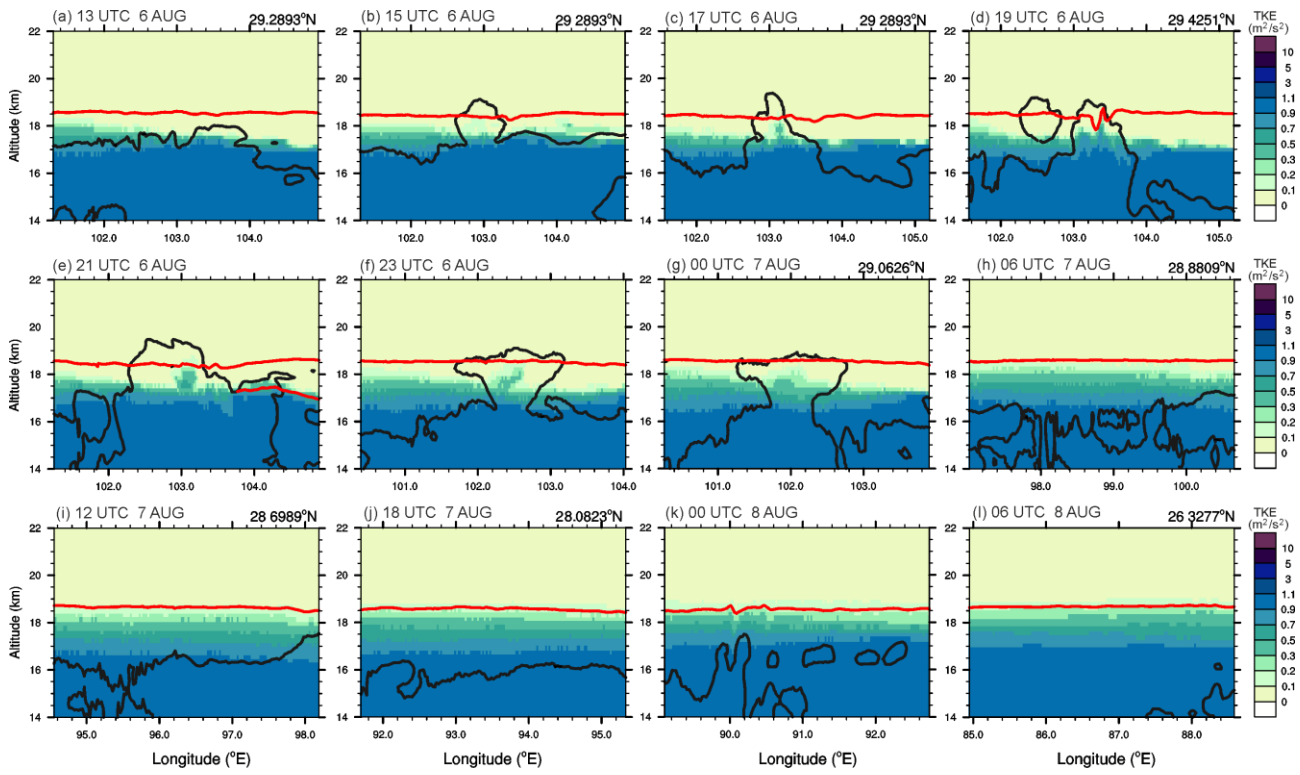
656  
657  
658  
659  
660

**Figure 7.** Same as Fig. 6 but for the ice content. The isentropic altitudes of 380 and 410 K are depicted by the red lines.



661  
662  
663  
664

**Figure 8.** Same as Fig. 6 but for the tracer (%). The isentropic altitude of 410 K is depicted by the red line. The changes of the tropospheric tracer by convective overshoots is marked by downward arrows.

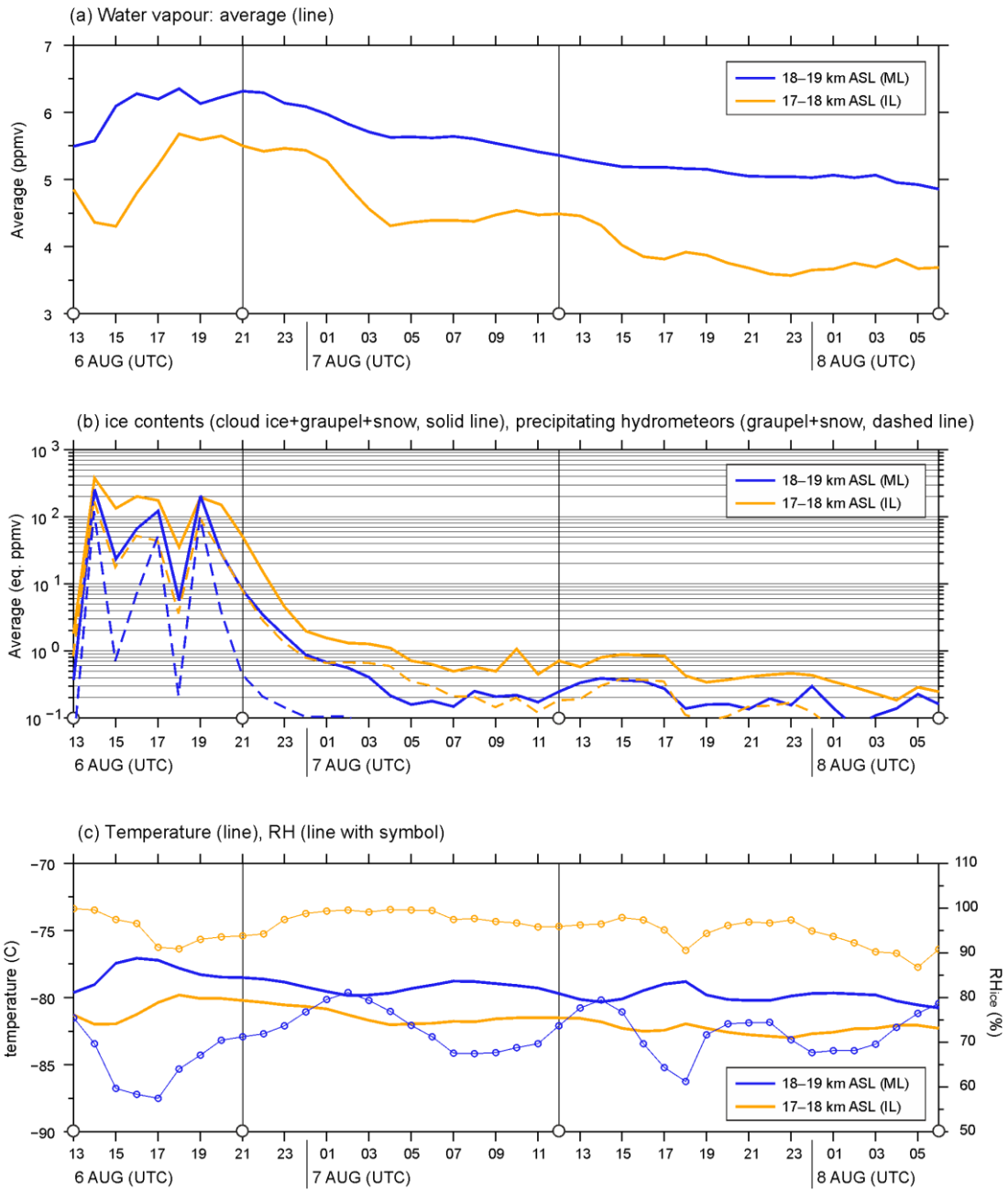


665

666

667 **Figure 9.** Same as Fig. 6 but for the TKE. The isentropic altitude of 410 K is depicted by the red line.

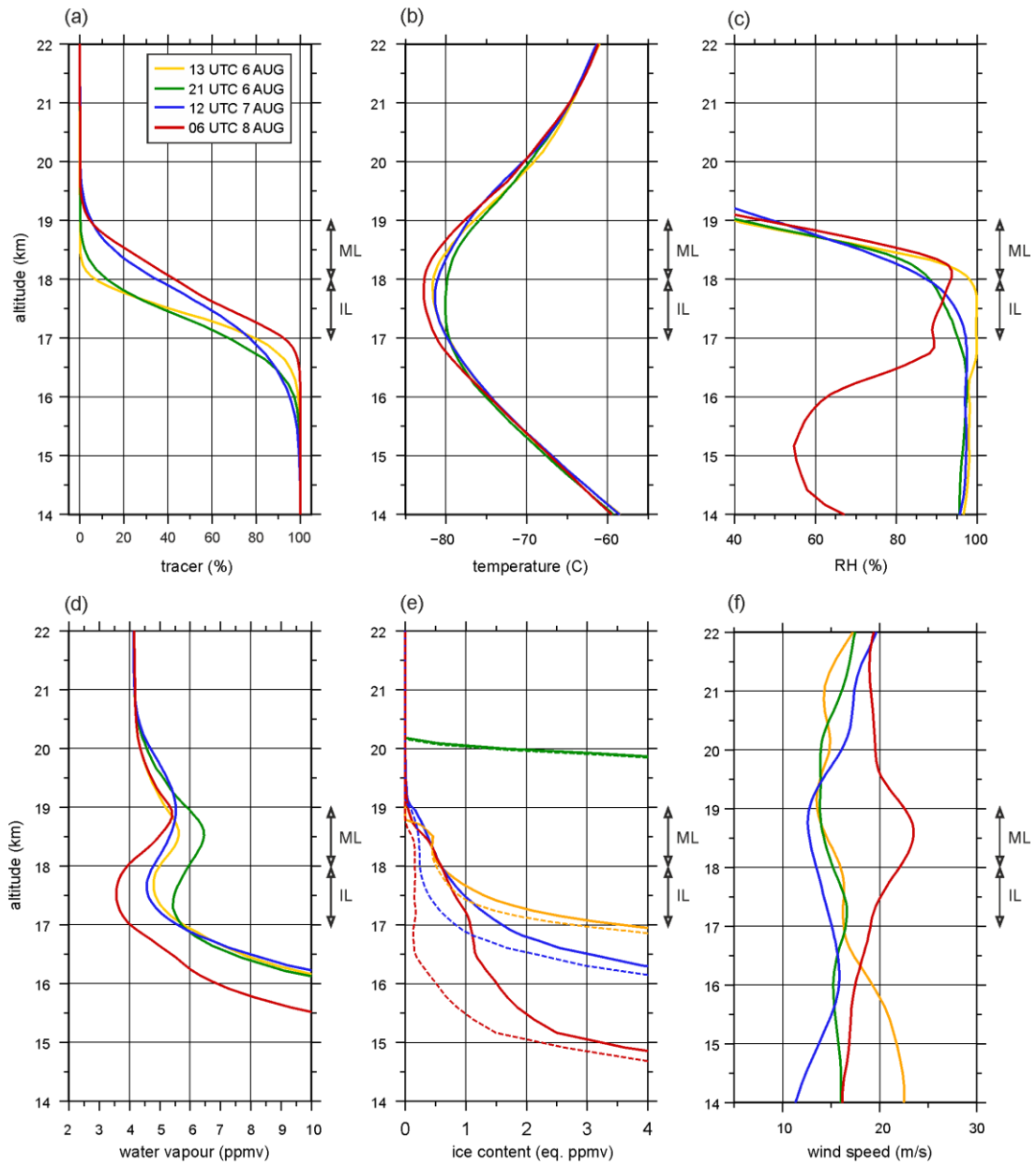
668



669

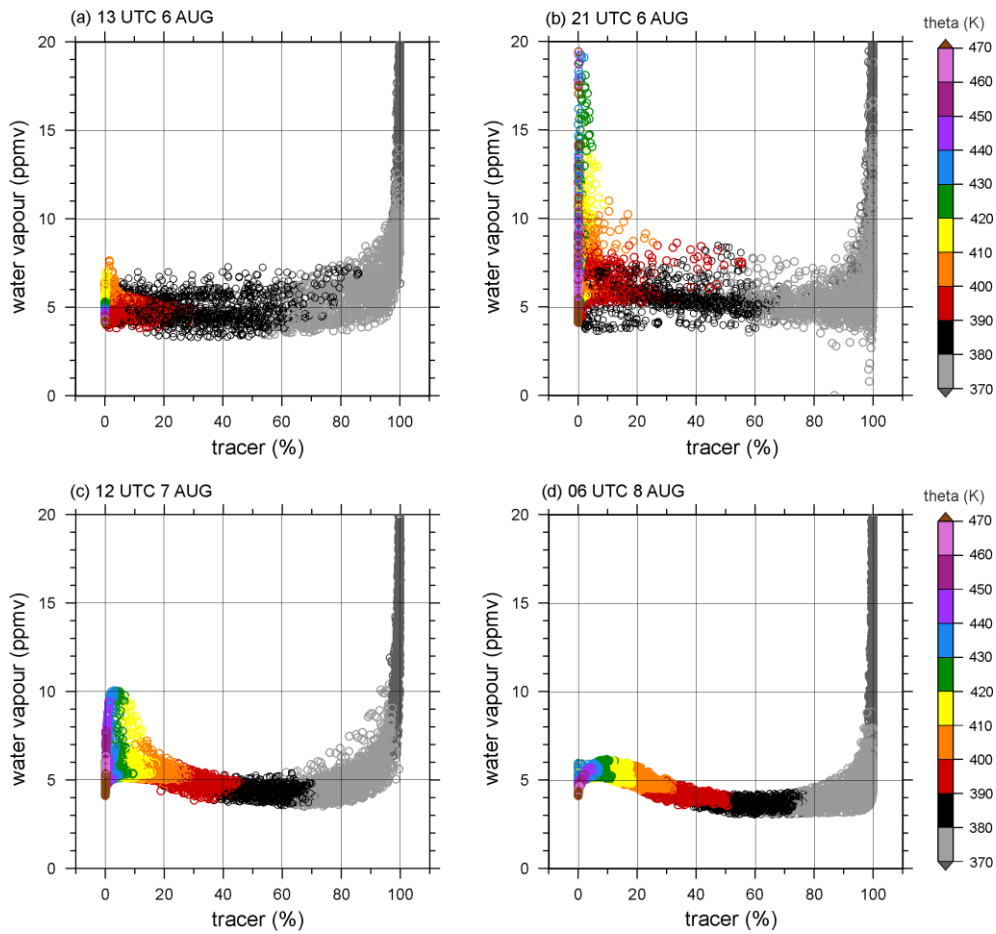
670 **Figure 10.** Hourly evolution of (a) averaged water vapour (line), (b) averaged ice content (solid line, sum of ice, graupel, and snow)  
 671 and the precipitating hydrometeor (dashed line, sum of graupel and snow), and (c) averaged temperature (line) and relative humidity  
 672 ( $RH_{ice}$ , thin line with circle) in the altitudes of 17–18 km (yellow lines) and 18–19 km (blue lines) ASL from 13:00 UTC on 6 August  
 673 to 06:00 UTC on 8 August 2017. The four analysis times are marked by open circles on the x-axis. Average and maximum values are  
 674 calculated in ML and IL.

675



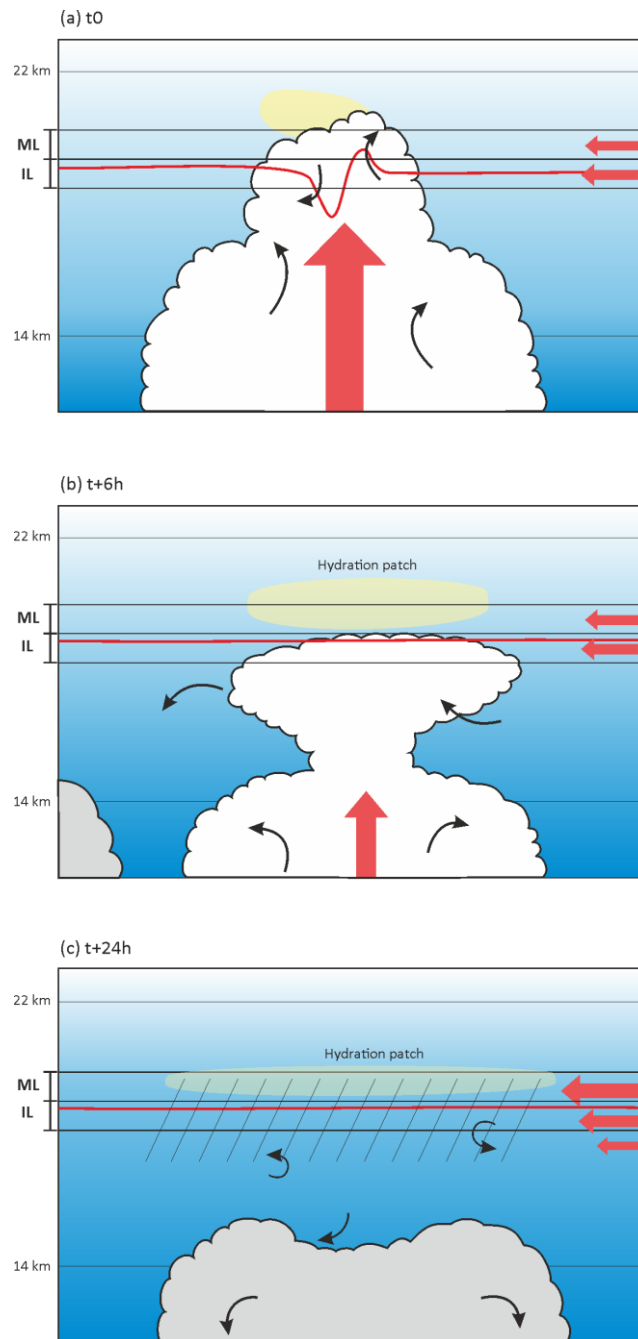
676

677 **Figure 11.** Vertical profiles of (a) tracer (%), (b) temperature (°C), (c) relative humidity (%), mixing ratios of (d) water vapour (ppmv),  
 678 (e) ice content (eq. ppmv), and (f) wind speed ( $\text{m s}^{-1}$ ) across the hydration patch along the trajectory at 13:00 UTC (yellow line), 21:00  
 679 UTC (green line) on 6 August, 12:00 UTC on 7 August (blue line), and 06:00 UTC (red line) on 8 August 2017. The layers of ML and  
 680 IL are marked by arrows. In (e), the ice content is depicted by solid lines, while the cloud ice are shown by dashed lines.



681

682 **Figure 12.** Mixing diagram using tropospheric tracer (%) and water vapour (ppmv) across the hydration patch in the altitudes between  
 683 14 and 22 km ASL along the trajectory at (a) 13:00 UTC on 6 August, (b) 21:00 UTC on 6 August, (c) 12:00 UTC on 7 August, and  
 684 (d) 06:00 UTC on 8 August 2017. The potential temperature (K) is shown with colour shading.



685

686

687 **Figure 13.** Schematic illustration summarising the hydration process in the TTL during flight #7 of the StratoClim 2017 field campaign.

688 (a) Mixing of the overshoots with the stratospheric air, (b) and (c) turbulent mixing of the hydration patch with the tropospheric air by

689 vertical wind shear. The bottom and top of the TTL, 14 and 22 km, and the moist layer (ML) and ice layer (IL) are represented by the

690 black solid line, and the 410 K isentropic altitude is represented by the red solid line. The main force in the TTL is marked by bold red

691 arrows, while the turbulent eddies in/around the developed and weakened overshoots are described by black arrows. The overreaching

692 water vapour above the cloud top level is indicated by a yellow ellipsoid in (a). The hydration patch is yellow-encapsulated in (a) and

693 (b), and the layer of dehydration by turbulent diffusion and ice microphysics is hatched in (c). The blue shades illustrate the

694 concentration of tropospheric air, showing the increased tropospheric air in the TTL by the turbulent mixing in (b) and (c).